JGR Oceans

RESEARCH ARTICLE
10.1029/2021JC017732

Historical Reconstruction of Subpolar North Atlantic Overturning and Its Relationship to Density

Vassil M. Roussenov[1], Richard G. Williams[1], M. Susan Lozier[2], N. Penny Holliday[3], and Doug M. Smith[4]

[1]Department of Earth, Ocean & Ecological Sciences, School of Environmental Sciences, University of Liverpool, Liverpool, UK, [2]School of Earth and Atmospheric Sciences, Georgia Institute of Technology, Atlanta, GA, USA, [3]National Oceanography Centre, Southampton, UK, [4]Met Office Hadley Centre, Exeter, UK

Key Points:

- Dominant eastern basin contribution to overturning in reconstructions for the subpolar North Atlantic in accord with recent observations
- Boundary density changes in the Irminger Sea connect to overturning changes over the eastern subpolar basin
- Localized buoyancy forcing over the Labrador Sea only enhances the overturning changes over the western side of the subpolar basin

Correspondence to:

V. M. Roussenov and R. G. Williams,
vassilr@liverpool.ac.uk;
ric@liverpool.ac.uk

Citation:

Roussenov, V. M., Williams, R. G., Lozier, M. S., Holliday, N. P., & Smith, D. M. (2022). Historical reconstruction of subpolar North Atlantic overturning and its relationship to density. *Journal of Geophysical Research: Oceans*, *127*, e2021JC017732. https://doi.org/10.1029/2021JC017732

Received 28 JUN 2021
Accepted 28 APR 2022

Author Contributions:

Conceptualization: Vassil M. Roussenov, Richard G. Williams, M. Susan Lozier
Formal analysis: Vassil M. Roussenov, Richard G. Williams, M. Susan Lozier, Doug M. Smith
Funding acquisition: Richard G. Williams
Investigation: Vassil M. Roussenov, Richard G. Williams, N. Penny Holliday, Doug M. Smith
Methodology: Vassil M. Roussenov, Doug M. Smith
Project Administration: N. Penny Holliday
Validation: Vassil M. Roussenov
Writing – original draft: Richard G. Williams

Abstract The connections between the overturning of the subpolar North Atlantic and regional density changes are assessed on interannual and decadal timescales using historical, data-based reconstructions of the overturning over the last 60 years and forward model integrations with buoyancy and wind forcing. The data-based reconstructions reveal a dominant eastern basin contribution to the subpolar overturning in density space and changes in the overturning reaching ±2.5 Sv, which are both in accord with the Overturning in the Subpolar North Atlantic Program (OSNAP). The zonally integrated geostrophic velocity across the basin is connected to boundary contrasts in Montgomery potential in density space. The overturning for the eastern side of the basin is strongly correlated with density changes in the Irminger and Labrador Seas, while the overturning for the western side is correlated with boundary density changes in the Labrador Sea. These boundary density signals are a consequence of local atmospheric forcing and transport of upstream density changes. In forward model experiments, a localized density increase over the Irminger Sea increases the overturning over both sides of the basin due to dense waters spreading to the Labrador Sea. Conversely, a localized density increase over the Labrador Sea only increases the overturning for the western basin and instead eventually decreases the overturning for the eastern basin. Labrador Sea density provides a useful overturning metric by its direct control of the overturning over the western side and lower latitudes of the subpolar basin.

Plain Language Summary The overturning in the subpolar North Atlantic is reconstructed from historical data over the last 60 years. These reconstructions are consistent with ongoing observational measurements confirming that the overturning is dominated by an eastern basin contribution from between Greenland and Scotland. This overturning response is strongly correlated with density changes in the Labrador Sea and Irminger Sea. The boundary density for the Irminger Sea provides a direct control of the overturning over the eastern side of the basin and similarly, the boundary density around the Labrador Sea directly affects the overturning over the western side of the basin. Model experiments are conducted using localized forcing, showing that a density increase over the Irminger Sea enhances the overturning over the entire basin, while a density increase over the Labrador Sea instead eventually decreases the overturning for the eastern basin through a southern influx of warmer and lighter water.

1. Introduction

There is a widespread view that the meridional overturning in the subpolar North Atlantic is determined by processes acting within the Labrador Sea (Delworth et al., 1993; Eden & Willebrand, 2001) with the strength of the overturning associated with density changes in the Labrador Sea (Ortega et al., 2017; Robson, Hodson, et al., 2014; Robson et al., 2016). However, continuous observations of the overturning in density space from the Overturning in the Subpolar North Atlantic Program (OSNAP, Lozier et al., 2017) have recently challenged this viewpoint of a dominant Labrador Sea contribution by revealing an overturning contribution that is much larger over the eastern side of the subpolar basin, compared with the western contribution (Li et al., 2021; Lozier et al., 2019). There is a question of how to reconcile these two perspectives.

The inferences from the OSNAP observational program are so far based on 4 years of continuous observations (Li et al., 2021), so there is a practical issue of how representative the OSNAP findings are for longer periods. In addition, there is a question as to how the subpolar overturning connects to the regional density distribution, including over the Labrador Sea, the Irminger Sea, and the Iceland Basin. The regional connections between

Writing – review & editing: Vassil M. Roussenov, Richard G. Williams, M. Susan Lozier, N. Penny Holliday, Doug M. Smith

the subpolar overturning and regional density changes may be due to a combination of the local imprint of the atmospheric forcing associated with the North Atlantic Oscillation (NAO) (Robson, Hodson, et al., 2014) and/or through the gyre-scale redistribution of upstream density anomalies (Menary et al., 2020).

In this study, data-based reconstructions of the annual overturning in density coordinates are used to assess how representative the OSNAP analyses of 4 years of monthly overturning are in time and space (Section 2). The historical analyses provide an annual context for the overturning over the last 60 years as well as a comparison between the meridional overturning across latitude circles. The zonally integrated geostrophic velocity across the basin is connected to boundary contrasts in Montgomery potential along density surfaces for different composites of the NAO. The data-based reconstructions reveal how the western and eastern contributions to OSNAP overturning correlate with regional density changes. Forward model integrations are then performed (Section 3) to identify how regional density changes and associated overturning signals are induced by localized buoyancy and wind forcing patterns associated with the NAO. This combination of historical data reconstruction and forward model integrations is then used to test the extent to which the Labrador Sea density provides a useful metric of how the subpolar overturning varies (Li et al., 2019) and the implicit causality contained within this relationship (Section 4).

2. Data-Based Reconstructions of the Overturning

2.1. Methods

In order to address how representative the OSNAP measurements are, we estimate the overturning from historical temperature and salinity data assimilated into a dynamical model (Williams et al., 2014, 2015) similar to previous diagnostic studies for the North Atlantic (Greatbatch et al., 1991; Mellor et al., 1982):

1. Historical temperature and salinity changes are obtained from the Met Office statistical ocean reanalysis (MOSORA, Smith et al., 2015). This is a global optimal interpolation of the available hydrographic data and recent Argo data from 1950 to 2020 with a horizontal resolution of 1.25° and with 20 vertical levels. Data sparse regions are filled by extrapolating from the observational data using covariances from a perturbed physics ensemble of the Hadley Centre Model (HadCM3) and then iteratively updated with observations (Smith et al., 2015).
2. The global Massachusetts Institute of Technology (MIT) general circulation model (Marshall et al., 1997) is initialized with the annual mean temperature and salinity data based on monthly means from Hadley Centre analyses of temperature and salinity data, interpolating the slightly coarser historical data analyses onto a 1° grid with 23 vertical levels over the globe. This global MIT model is integrated forward with an initial 1-month spin-up and then a further 12 months to cover an annual cycle. This dynamical adjustment allows the circulation to spin up that is dynamical consistent with the density distribution. The model includes forcing from monthly mean wind stresses from European Centre for Medium-Range Weather Forecasts (ECMWF) for each year (using ERA40 for years 1960–1978 and ERA Interim for 1979–2020), so including the Ekman contribution to the overturning. The dynamical adjustment does not include explicit surface heat or freshwater fluxes, but includes a weak artificial relaxation of temperature and salinity to the initial annual-averaged temperature and salinity data on a timescale of 36 months, which acts to minimize model drift. The effect of the mesoscale eddy transport is taken into account by using the Gent and McWilliams (1990) sub-grid-scale mixing parameterization.
3. This initialization and assimilation procedure is repeated for each separate year from 1960 to 2020. The subsequent changes in overturning are then evaluated from these dynamically adjusted velocities and densities covering an annual cycle.

This dynamical assimilation approach avoids the difficulty of model drift that occurs with integrations over several decades and by design, the overturning circulation is dynamically consistent with the density distribution. There are two important caveats to this procedure: first, the assimilated products only provide annual estimates of the overturning, so omit seasonal variability and second, they are based on a dynamical assimilation on a 1° grid, so omit dynamical effects of finer-scale mesoscale circulations. Despite these caveats, this approach has proven useful in assessing decadal changes in ocean basin-scale overturning and heat content (Lozier et al., 2010; Williams et al., 2014, 2015); see model tests of our approach comparing our density-based reconstructions of the overturning and the actual model overturning from GECCO for 22-year periods (Lozier et al., 2010) and

from ECCO for two 5-year periods (Williams et al., 2014). Our dynamical assimilation approach is the same as reported in Williams et al. (2015), apart from including additional years of data input.

The overturning is calculated in density coordinates as there are strongly sloping density surfaces across the subpolar basin (Holliday et al., 2018) that complicate the interpretation of the overturning in depth space. The overturning in density space naturally combines the overturning in depth space and the horizontal gyre circulation together. The overturning streamfunction, $\psi(\sigma)$ in *S*v, is estimated in density space following the OSNAP program (Li et al., 2021; Lozier et al., 2019) by

$$\psi(\sigma) = \int_{s_w}^{s_e} \int_{\sigma_{min}}^{\sigma_{max}} V_{\perp}(s,\sigma) \mathrm{d}\sigma \mathrm{d}s, \tag{1}$$

where $V_{\perp}(s,\sigma)$ is the volume flux per unit length per unit density normal to the section, given by the product of the normal velocity $v_{\perp}(s,\sigma)$ and layer thickness, $h(s,\sigma)$ divided by the density bin, with a northward flux and velocity taken to be positive, s_e and s_w are the eastern and western ends, respectively, of the section with s measuring the distance along the section (with positive in the eastward direction), and σ_{min} σ_{max} are the minimum and maximum potential densities, respectively, for the overturning and with the potential density referenced to the sea surface. The minimum density is always the lightest density along the section and the maximum density may either be chosen to be fixed or is the density that provides the maximum value of the overturning streamfunction. The estimate of the overturning in density space from the OSNAP field program is only marginally changed when calculated using neutral densities (Lozier et al., 2019).

Observational arrays are designed to monitor the overturning in the Atlantic (McCarthy et al., 2020) across a coast-to-coast section by calculating the Ekman transport from atmospheric wind stress and measuring the geostrophic shear and bottom velocity or external model and ensuring an overall mass balance (Baehr et al., 2004; Hirschi & Marotzke, 2007; Li et al., 2017).

The variability of the overturning on annual timescales and longer is dominated by the geostrophic shear contributions (Hirschi & Marotzke, 2007), which has led to the focus on boundary end point monitoring of the density contributing to the overturning circulation. In Cartesian coordinates, the zonal integral of the meridional geostrophic velocity, $v_g = \frac{1}{\rho f}\frac{\partial P}{\partial x}\Big|_z$, across a basin is simply given by the east-west boundary contrasts in pressure at the same depth (Marotzke et al., 1999),

$$\int_{x_w}^{x_e} v_g(x,z)\mathrm{d}x = \frac{1}{\rho f}\left(P_e - P_w\right), \tag{2}$$

where ρ is a reference density, f is the Coriolis parameter, and P_e and P_w are the pressures on the eastern and western boundaries, respectively. The boundary pressures are themselves connected to the boundary densities via the hydrostatic balance.

For the subpolar gyre, a density-based view of the overturning is more appropriate than a depth-based view. Drawing upon how the geostrophic flow varies along isentropic surfaces in the atmosphere (Montgomery, 1937), the meridional geostrophic velocity, v_g, is connected to horizontal gradients of the Montgomery potential (m^2s^{-2}) where $M = \alpha P + gz$ (Bleck & Smith, 1990), α is the specific volume anomaly, P is pressure, and z is the depth of the specific volume anomaly surface. The Montgomery potential provides a geostrophic streamline along a specific volume surface,

$$v_g = \frac{1}{f}\frac{\partial M}{\partial x}\Big|_{\alpha},$$

so that the zonal integral of the meridional geostrophic velocity across a basin is then given by the east-west boundary contrasts in Montgomery potential evaluated along the same specific volume surface,

$$\int_{x_w}^{x_e} v_g(x,\alpha)\mathrm{d}x = \frac{1}{f}\left(M_e - M_w\right)_{\alpha}, \tag{3}$$

and M_e and M_w are the Montgomery potential on the eastern and western boundaries.

As the subpolar overturning in Equation 1 is evaluated in potential density coordinates, we choose to connect the geostrophic flow to the Montgomery potential along potential density surfaces referenced to the sea surface as an approximation to specific volume surfaces; this equivalence in using the Montgomery potential is not exact due to nonlinearities from the equation of state, including a term due to differences between the pressure on the potential density and the reference sea surface pressure (McDougall & Klocker, 2010). The Montgomery potential, $M = \alpha P + gz$, is evaluated in the following manner: (a) the density is evaluated from the gridded temperature and salinity data using the international thermodynamic equation of state (McDougall et al., 2009); (b) the density within the water column directly alters the specific volume anomaly α and the height of the potential density surface, z; (c) the pressure P is made up of a sea surface height contribution and a depth-varying contribution depending upon the density distribution from hydrostatic balance. This calculation of the Montgomery potential is performed for each potential density layer. The potential density surfaces are close to the specific volume surfaces over the upper water column, so that the Montgomery potential then defines the geostrophic flow in density coordinates as applied in an isopycnic circulation model (MICOM, Bleck and Smith, 1990). The zonal integral of the meridional geostrophic velocity across a basin is then given by the east-west boundary contrasts in Montgomery potential evaluated along the same potential density surface,

$$\int_{x_w}^{x_e} v_g(x,\sigma)\mathrm{d}x = \frac{1}{f}\left(M_e - M_w\right)_\sigma , \tag{4}$$

where σ defines the density surface. If the density surfaces outcrop or ground, then the boundary value of the Montgomery potential within the zonal integral in Equation 4 is taken at the point of the outcrop or grounding point rather than at the western or eastern boundary. For density surfaces that outcrop, the Montgomery potential is controlled by the surface pressure. This calculation of the Montgomery potential is used to interpret the changes in the velocity structure for potential density surfaces in the upper 1 km along the OSNAP sections for both the climate mean and different states of the NAO (Section 2.4).

2.2. Historical Reconstruction of the Overturning Over the Subpolar Gyre

Our historical data-based reconstruction of the overturning defined in terms of density using Equation 1 strongly varies over the subpolar latitudes, ranging from a subpolar maximum of 19.39 ± 0.81 Sv at 54°N to 14.41 ± 0.65 Sv at 60°N (Figure 1a). The subpolar anomalies in the density-based overturning reach up to ±2.5 Sv and are negative for years 1965–1970, changing to positive for 1975–2000, and returning to negative for 2000–2017. This variability in the subpolar overturning in density space compares with a strengthening in the subpolar overturning in depth space of typically 1 Sv during 1980–2000 compared with 1950–1970 (Lozier et al., 2010). The temporal changes in the meridional overturning from the subtropical gyre to the subpolar gyre lead in the early 1970s to a decrease in northward heat transport and loss in subpolar heat content and an increase northward in the mid-1990s and a gain in subpolar heat content (Williams et al., 2015); see studies revealing this subpolar loss and gain of heat using an ocean model by Robson et al. (2012) and analyses of a coupled model prediction system by Robson, Sutton, and Smith (2014).

The changes in the overturning include regions where there appears to be signals propagating southward with latitude from 65°N to 58°N and regions where there appears to be a very coherent response with latitude from 40°N to 58°N (Figure 1b). The overturning anomalies often have the opposite sign between the subtropical and subpolar gyres. There is often a break in the latitudinal communication between the gyres at around 45°N as revealed on interannual to decadal timescales in ocean model experiments using Cartesian and isopycnal coordinates (Bingham et al., 2007; Buckley & Marshall, 2016; Zou et al., 2020).

Our aim is now to explore the subpolar overturning signals and their connections to boundary density by focusing on reconstructions for the OSNAP observing system (Lozier et al., 2017). The OSNAP observing system running coast to coast across the subpolar North Atlantic (Figure 2) reveals an overturning in density space with a mean and standard deviation for annual means of 16.6 ± 0.8 Sv over the period 2014–2018 (Li et al., 2021; Lozier et al., 2019). The annual standard deviation is reported here rather than the smaller standard error as the relevant issue is how representative a 4-year snapshot is compared to our 60-year reconstructions. The overturning is dominated by the contribution from the eastern side of the basin, OSNAP east, running from the southeastern tip of Greenland to the Scotland shelf, reaching 16.8 ± 1.0 Sv. The overturning contribution on the western side

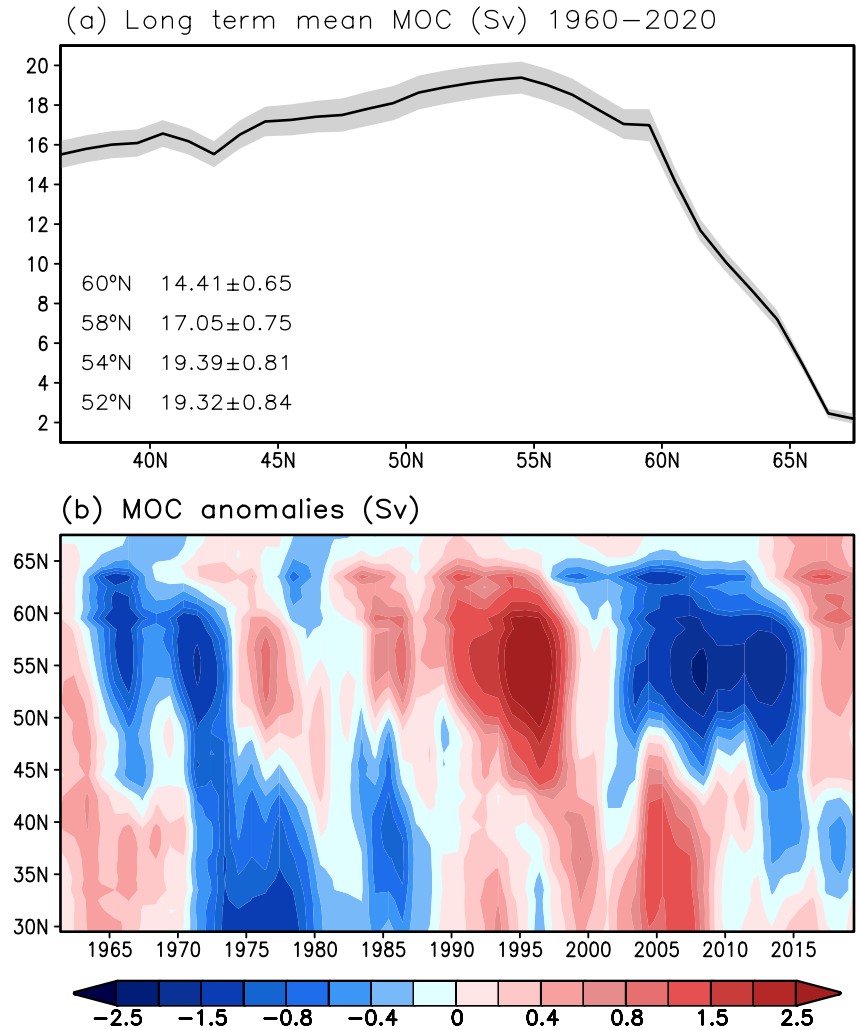

Figure 1. (a) Historical data-based model reconstructions of the meridional overturning in density space (Sv) versus latitude from annual estimates from 1960 to 2020 (mean is black line and gray is one standard deviation). Numbers show the long-term averages and standard deviations based on annual values. (b) The MOC anomalies defined in density space for year versus latitude with a 3-year running mean using a fixed maximum density limit, $\sigma_{max} = 27.7$ in Equation 1.

of the basin, OSNAP west, running from the southwestern Labrador shelf to the southwestern tip of Greenland, instead only reaches 2.6 ± 0.5 Sv.

The long-term estimates of the overturning from the data-based reconstructions from 1960 to 2020 (Figure 3, black line) are consistent with the OSNAP analyses from 2014 to 2018 (Table 1); there is an overturning across the entire section of 16.0 ± 0.8 Sv with a dominant contribution from the eastern side of the basin of 16.49 ± 0.62 Sv and a weaker contribution on the western side of 3.42 ± 0.41 Sv (where again the mean and standard deviations are reported). The western contribution is larger in the data-based reconstruction than that measured in OSNAP, but the difference is within the variability indicated by the standard deviations. In agreement with the observations, there is a larger contribution and variability in the overturning for the eastern section than for the western section. When diagnosed for the same period as the OSNAP analyses from 2014 to 2018, the reconstructions for the overturning are only slightly altered (Table 1), reaching 15.94 ± 0.43 Sv across the entire section, 16.86 ± 0.56 Sv on the eastern section and 3.46 ± 0.20 Sv on the western section.

The reconstruction for the overturning is evaluated using a variable maximum density limit, σ_{max}, chosen to maximize the overturning using Equation 1. This maximum density limit, σ_{max}, varies between 27.5 and 27.6 for the eastern section and increases from 27.7 to 27.8 for the western section and is a compromise of 27.6–27.7 for the full line. By design, these choices of σ_{max} identify the maximum overturning across an individual section, but have

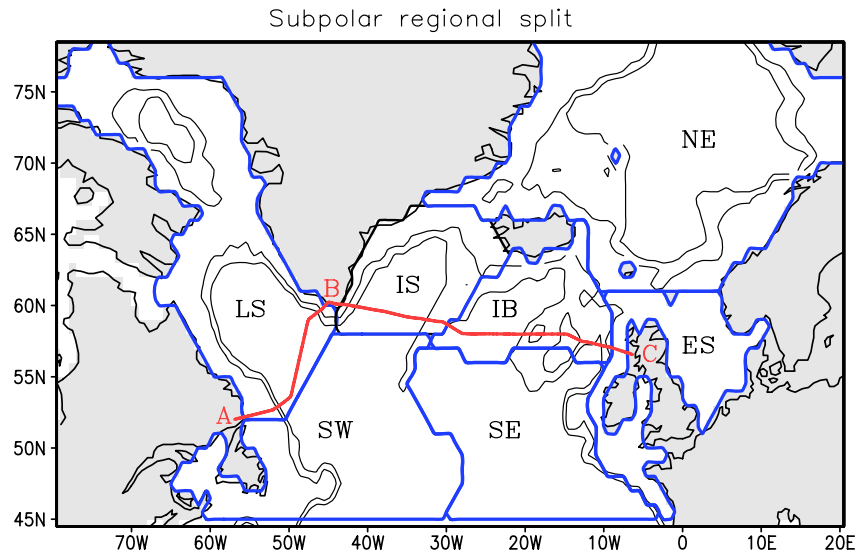

Figure 2. Subpolar domain of the study: OSNAP west and east sections from A to B and B to C, respectively (red lines). The density responses are separated into shallow and deep responses relative to the shoreward side of the 2-km depth contour (black contours for depths of 1 and 2 km). Our analysis focuses on the regional response involving the Labrador Sea (LS) and the Irminger Sea (IS), and their connections with upstream regions of the Iceland Basin (IB) and the southeast subpolar gyre (SE), and the downstream region of the southwest subpolar gyre (SW). In our model experiments, the north east Atlantic and Nordic Seas (NE) and the northwest European shelf (ES) are included for completeness.

the deficiency that the overturning crossing the full line is not equal to the sum of the overturning contributions from the eastern and western sections (Table 1). This mismatch is due to some of the waters in the lower limb of OSNAP east being further densified in the Labrador Sea (Lozier et al., 2019), so that their transport contributions appear in different density classes for each section and are counted twice when summing over both sections.

Alternatively, the overturning may be evaluated using the same maximum density limit, σ_{max}, across all sections, which leads to reduced estimates of the overturning (Table 1 for σ_{max} of 27.6 or 27.7), but with the overturning across the full line being the sum of the overturning contributions from the western and eastern sections. When the same σ_{max} is chosen, then the variability is comparable from both the western and eastern sections (Figure A1 for $\sigma_{max} = 27.7$).

2.3. Connections Between the Overturning Across the OSNAP Line and the Meridional Overturning at Different Latitudes

The reconstruction of the overturning over OSNAP east is strongly correlated with the meridional overturning across 60°N at zero lag (Figure 3, blue line; Figure 4, black lines), reaching 0.94 and 0.83 for the eastern section and the full line (Table 2). The overturning for OSNAP east is only weakly correlated with the meridional overturning at latitudes further south than 57°N (Figure 4a), including timescale lags of up to 6 years, although the correlations do rise if a 3-year smoothing is applied (Figure 4c). There are high, negative correlations between the overturning at OSNAP east and the meridional overturning in the subtropical gyre at lags from 0 to 3 years. These subtropical signals are likely to be a consequence of the atmospheric forcing in the subtropical gyre that are out of phase with the atmospheric forcing along OSNAP east.

The reconstruction of the overturning over OSNAP west is strongly correlated with the meridional overturning across the western section of 60°N and is also correlated at lower latitudes in the subpolar gyre, reaching 0.93 for the western section, 0.64 for 52°N, and 0.51 for 46°N for zero lag (Table 2). Further south at 40°N, there is an increased correlation between OSNAP west with lags for the lower latitude response of 2–3 years (Figure 4b). The lagged correlations between the overturning at OSNAP west and the low latitudes significantly increase if a 3-year smoothing is applied (Figure 4d). This response within the subpolar gyre is consistent with the overturning signals being communicated southward by an adjustment of boundary density signals.

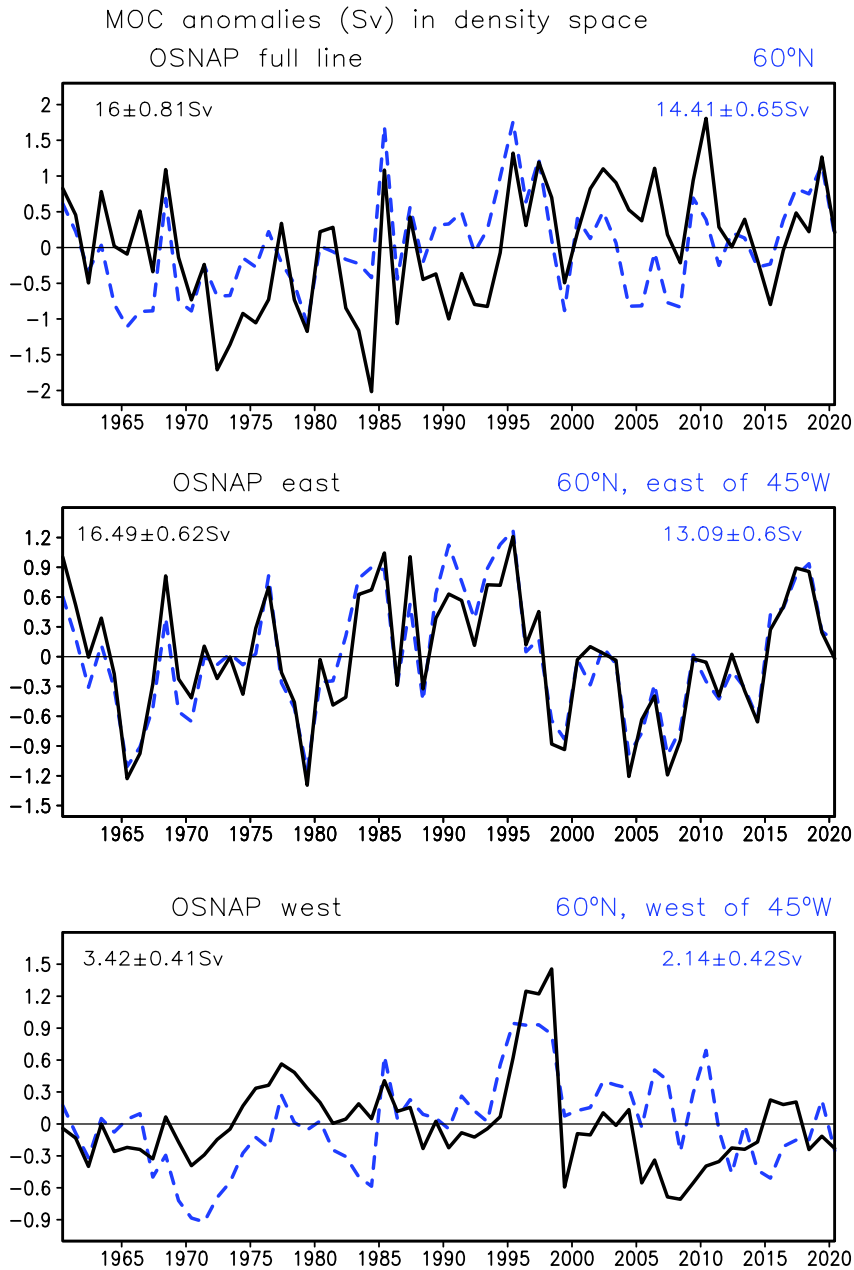

Figure 3. Historical data-based model reconstructions of the overturning in density space (Sv) across the OSNAP full line (black) together with the meridional overturning across 60°N (blue dashed) from 1960 to 2020: (a) for the full line, (b) east of 45°W, and (c) west of 45°W. Numbers show the long-term averages and standard deviations based on annual values (also reported in Table 1). Following the OSNAP protocol, estimates for the western and eastern sections are defined for different choices in the maximum density limit, σ_{max} in Equation 1; see Appendix Figure A1 for the time series of the overturning using a fixed maximum density limit, $\sigma_{max} = 27.7$.

There are also low-latitude signals where the subtropics are correlating with OSNAP west with a maximum correlation of 0.4 on lagged timescales of 5 years rising to 0.5 for smoothed data (Figures 5b and 5d). This subtropical signal does not strongly vary with latitude from 20°N to 35°N and might either reflect an imprint of changing atmospheric forcing or a possible propagating feature from the subpolar gyre. From the observational data alone, it is difficult to separate these two processes, an ocean internal communication to far-field forcing versus a local response to atmospheric forcing. For example, temporal changes in the pattern of wind forcing associated with the NAO may give interannual to decadal changes in sea surface temperature, which are not necessarily advected

Table 1
Observational and Our Data-Based Modeling Estimates of the Overturning (Sv) Across Full Line, West, and East Lines Using Either a Variable or Fixed Maximum Density Limit

	Full line	West of 45°W	East of 45°W
Observations from OSNAP for 2014–2018 using variable density for maximum overturning (using a variable σ_{max}) from Li et al. (2021)	16.6 ± 0.8	2.6 ± 0.5	16.8 ± 1.0
Data-based model reconstruction for 1960–2020 using the OSNAP protocol for maximum overturning (using a variable σ_{max})	16.00 ± 0.81	3.42 ± 0.41	16.49 ± 0.62
Data-based model reconstruction for 2014–2018 using the OSNAP protocol for maximum overturning (using a variable σ_{max})	15.94 ± 0.43	3.46 ± 0.20	16.86 ± 0.56
Data based reconstruction for 1960–2020 for the overturning using a fixed maximum density limit of $\sigma_{max} = 27.6$	15.95 ± 0.8	0.25 ± 1.5	15.71 ± 1.1
Data based reconstruction for 1960–2020 for the overturning using a fixed maximum density limit of $\sigma_{max} = 27.7$	13.95 ± 1.04	2.71 ± 0.84	11.24 ± 0.88
Overturning response for NAO+ years (Figure 8a, red for 16 years) for fixed maximum density limit, $\sigma_{max} = 27.7$	1.56	0.44	1.12
Overturning response for NAO− years (Figure 8a, blue for 12 years) for fixed maximum density limit, $\sigma_{max} = 27.7$	−0.55	−0.16	−0.39

Note. The overturning is estimated in density space along the model OSNAP line. The mean and standard deviation for annual means are included as well as characteristic values for different atmospheric states, NAO+ and NAO−.

at the surface, but instead represent a local response to the time-varying wind forcing (Visbeck et al., 1998) and/or a subsurface advective pathway (Foukal & Lozier, 2016). In addition, on multi-decadal timescales, the effect of changes in atmospheric wind forcing can lead to opposing sign anomalies in the meridional overturning over the subtropical and subpolar gyres (Lozier et al., 2010; Williams et al., 2014; Zou et al., 2020). This competition of local and far-field responses to atmospheric forcing is explored later in regionally forced model experiments in Section 3.

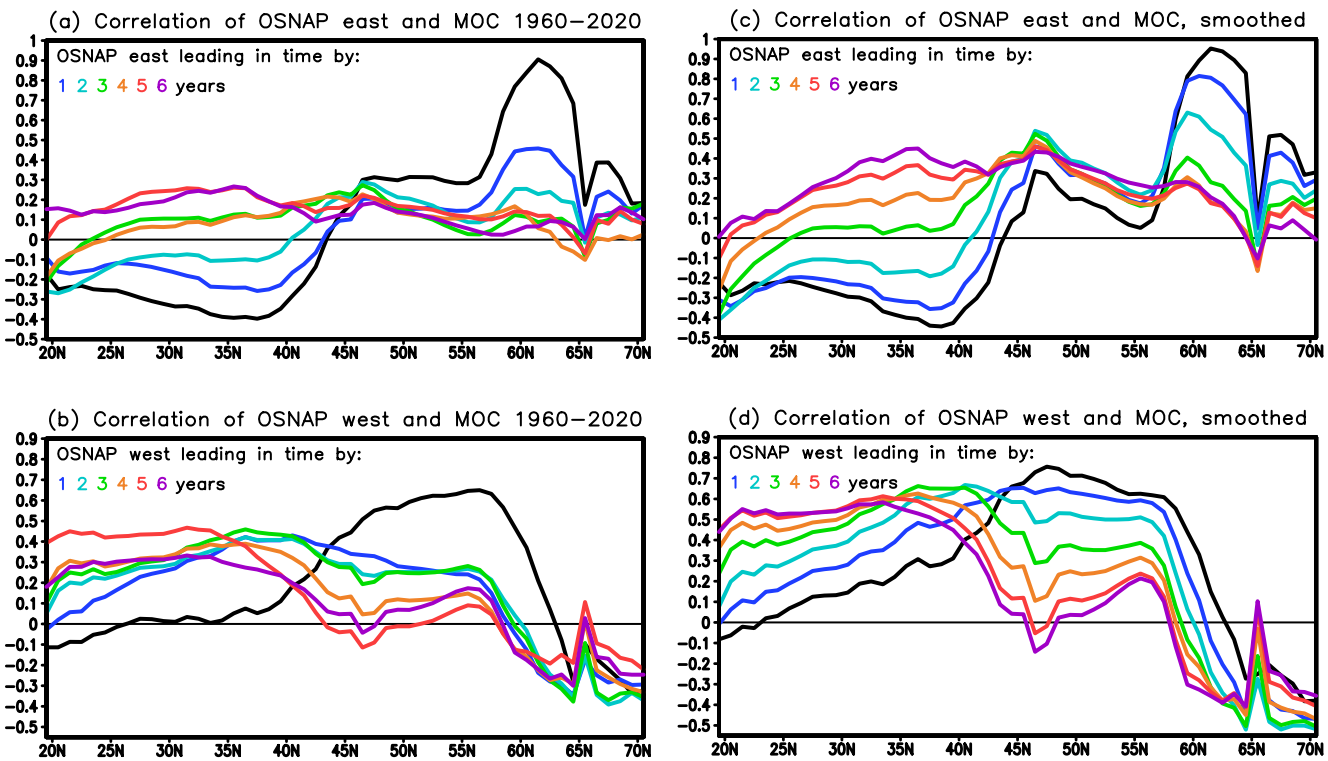

Figure 4. The lagged correlations between annual time series for (a), (c) the overturning for OSNAP east and the meridional overturning at each latitude and (b), (d) the overturning for OSNAP west and the meridional overturning at each latitude. The lagged correlations are shown both for unsmoothed time series (a), (b) and with a 3-year smoothing window (c), (d). The black line is for zero lag and blue to red lines for lags 1–6 years, where a lag denotes a later latitudinal response to the changes on the OSNAP sections.

Table 2
Correlations Between Overturning for OSNAP East and OSNAP West With the Meridional Overturning for 60°N, 52°N, and 46°N Latitude Circles

OSNAP east	60°N east of 45°W	**0.94**
	60°N full line	**0.83**
	52°N full line	0.30
	46°N full line	0.30
OSNAP west	60°N west of 45°W	**0.93**
	60°N full line	*0.41*
	52°N full line	**0.64**
	46°N full line	**0.51**

Note. Correlations are zero lag based on historical data-based reconstructions for annual estimates using unsmoothed time series from 1960 to 2020. Values of at least 99% confidence of 0.44 are in bold and at 98% confidence of 0.32 in italics.

2.4. Changes in the Overturning Across the OSNAP Lines Connected to Different States of the North Atlantic Oscillation

The overturning record is assessed in terms of the connection to the NAO, using a station-based index (Hurrell, 2013), with a magnitude threshold of 1.8 used to define annual composites of NAO+ states for 16 years and NAO− states for 12 years (Figure 8a). The overturning across the OSNAP full line is increased during NAO+ by 1.56 Sv and reduced during NAO− by −0.55 Sv with similarly signed changes in the western and eastern sides of the basin (Table 1). Over OSNAP east, there is an increase in the density reaching 0.05 kg m^{-3} over the upper 800 m over the western side of the section during NAO+ states relative to the climate mean and conversely, there is a similar decrease in the density during NAO− states (Figures 5a, 5c, and 5e). The northward geostrophic shear is then enhanced and acts to increase the meridional overturning during the NAO+ state and conversely is decreased during NAO− states. This response is consistent with subpolar gyre cyclonic circulation being enhanced during NAO+ and weakened during NAO− (as indicated by the anomalous patterns in sea surface height in Figure A2).

In density coordinates, the geostrophic flow may be approximated by the boundary contrasts in Montgomery potential along potential density surfaces, where the Montgomery potential, $M = \alpha P + gz$, is determined from the density within the water column and the sea surface height (Section 2.1). For OSNAP east in the climate mean, there is a westward decrease in the Montgomery potential along σ surfaces from 27.3 to 27.7, which is consistent with a northward geostrophic flow (Figure 5b). The average geostrophic velocity along the 27.6 surface is northward from Equation 4 due to the Montgomery potential on the western boundary being less than that on the eastern boundary (Figure 5g). For NAO+ states, the Montgomery potential anomaly decreases westward along σ surfaces from 27.3 to 27.7, implying a stronger northward geostrophic flow and a stronger meridional overturning (Figure 5d). For NAO− states, the Montgomery potential anomaly increases westward along these σ surfaces from 27.3 to 27.7, implying a weakening in the northward geostrophic flow and a weaker meridional overturning (Figure 5f). Accordingly, along the 27.6 surface, during a NAO+ state, the average northward geostrophic flow is enhanced over the section with a negative Montgomery potential anomaly on the western boundary and conversely, the opposing response occurs for a NAO− state (Figure 5h, blue and red lines).

The geostrophic flow responses are more complex over OSNAP west, but can still be understood in terms of the contrasts in Montgomery potential. In the climate mean, there is a north-westward flow over the Greenland side of OSNAP west changing to a south-westward flow over the Labrador side, which corresponds to the Montgomery potential being positive at the southern tip of Greenland, negative over most of the Labrador Sea and either weakly negative for denser surfaces or weakly positive for lighter surfaces over the southwestern boundary of the Labrador Sea (Figure 5b). For NAO+ states, the Montgomery potential anomaly is negative (Figures 5d and 5h) with a more negative value on the southwestern end compared with the northeastern end, implying a slight increase in the northwestward overturning across the section. For NAO− states, the Montgomery potential anomaly is positive (Figures 5f and 5h) with a more positive value on the northeastern end compared with the southwestern end, implying a slight decrease in the northwestward overturning across the section.

These changes in the Montgomery potential then reveal similarly signed changes in the geostrophic velocities contributing to the overturning for OSNAP west and east with a larger contribution from OSNAP east for both NAO+ and NAO− states, consistent with the volumetric diagnostics in Table 1. The geostrophic contribution to the overturning in Sv may be estimated from the following procedure: (a) evaluating the zonal integral of the product of geostrophic velocity and layer thickness, given by $\int_{x_w}^{x_e} v_g(x,\sigma)h(x,\sigma)\,dx$, for each density layer, and (b) summing over each of the density layer contributions, $\sum_{\sigma_{min}}^{\sigma_{max}} \int_{x_w}^{x_e} v_g(x,\sigma)h(x,\sigma)\,dx$ from the minimum to the maximum potential densities for the overturning following Equation 1, where $h(x,\sigma)$ is the layer thickness and $v_g(x,\sigma)$ is the geostrophic velocity, estimated from the west-east gradient in the Montgomery potential, $v_g = (1/f)\partial M/\partial x$. This Montgomery-based estimate of the overturning is 3.21 Sv for OSNAP west and 16.44 Sv for OSNAP east for a climate mean, very close to the corresponding direct diagnostics of 3.42 Sv for OSNAP west and 16.49 Sv for OSNAP east in Table 1.

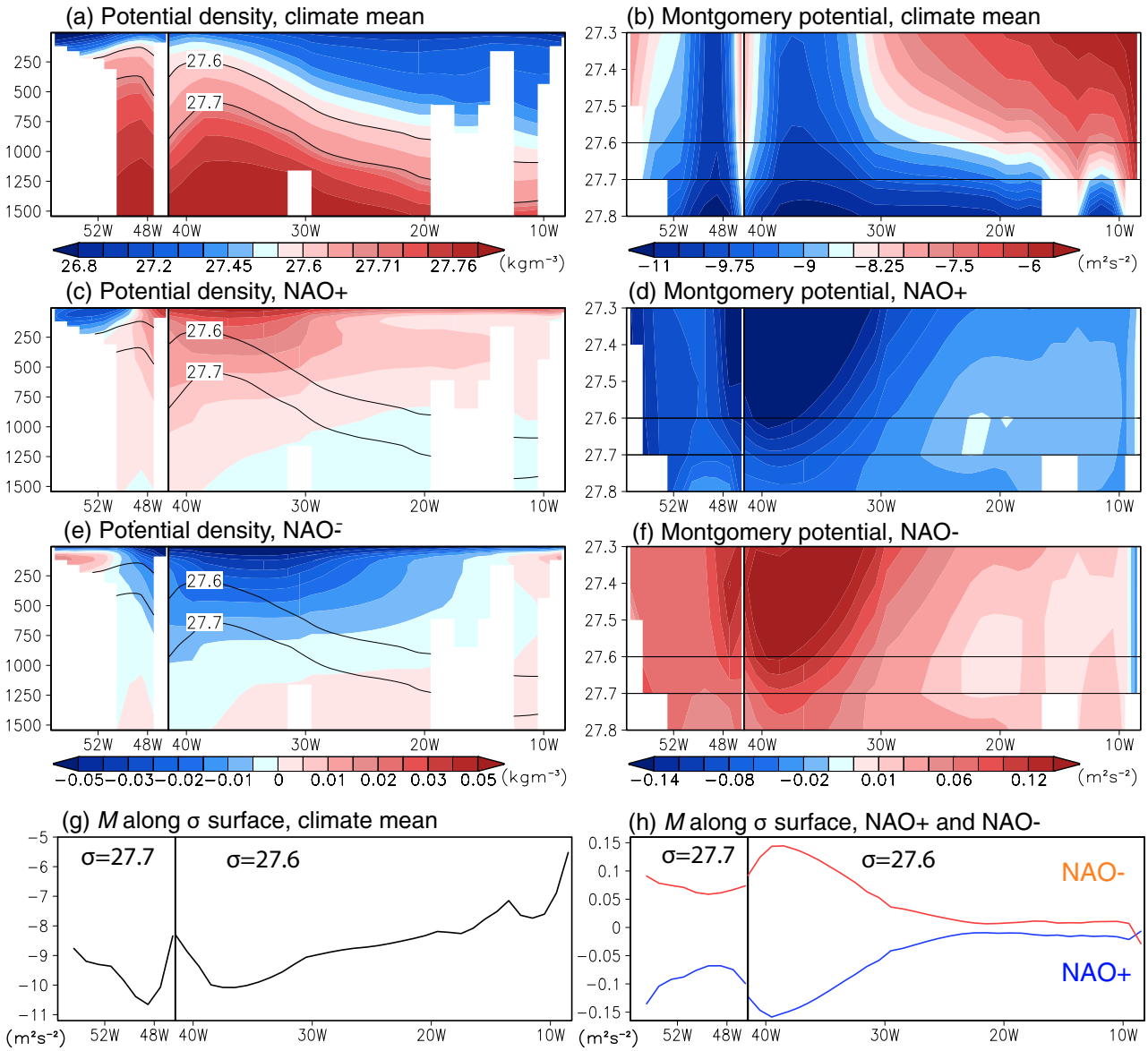

Figure 5. Combined OSNAP west and east sections for potential density σ surfaces (kg m^{-3}) versus depth and Montgomery potential (m^{2}s^{-2}) versus σ from our data-based diagnostics for a climate mean from years 1960 to 2020 in (a, b), and their anomalies for a composite of NAO+ states in (c, d) and NAO− states in (e, f). The Montgomery potential (m^{2}s^{-2}) versus longitude along the $\sigma = 27.6$ surface for OSNAP east and 27.7 surface for OSNAP west for the climate mean in (g) and the anomalies for the NAO+ (blue line) and NAO− (red line) composites in (h). In panels (a–f), the σ surfaces 27.6 and 27.7 surfaces are marked in black.

2.5. Connection Between Density and the Overturning

Given the imprint of the atmospheric forcing associated with NAO states on both the density distribution and the geostrophic circulation (Figures 5c–5f), now consider how the time series for the meridional overturning connects to the density distribution for this data-based reconstruction. In these historical reconstructions, the overturning for OSNAP east correlates with regional density anomalies in the Irminger Sea with a correlation coefficient ranging from 0.44 on the boundary and 0.56 for the southeast Irminger Sea at zero lag in Table 3. Maps of the correlation between the time series for the overturning for OSNAP east and the regional density above the 27.6 surface reveal correlations greater than 0.3 and reaching 0.5 over the Irminger Sea at zero lag and a similar pattern for the meridional overturning across the eastern side of 60°N (Figures 6a and 6b). In comparison, Li et al. (2021), using 46 months of monthly OSNAP data, obtain a smaller correlation of 0.31 between the OSNAP east overturning and the same overturning metric calculated using variable velocity and density only at

Table 3
Correlations at Zero Lag Between the Overturning for OSNAP East and OSNAP West With the Regional Density Above the Potential Density Surfaces σ of 27.6 and 27.7, Respectively, Based on Historical Data-Based Reconstructions From 1960 to 2020

OSNAP east with density above 27.6	Iceland basin	**0.51**
	Irminger Sea boundary	**0.44**
	Irminger Sea interior	**0.51**
	Southeast Irminger Sea	**0.56**
	Labrador boundary	−0.23
	Labrador interior	0.07
OSNAP west with density above 27.7	Irminger Sea boundary	*−0.33*
	Irminger Sea interior	*−0.37*
	Labrador boundary including western and eastern ends of OSNAP west	**0.62**
	Labrador interior	0.24
	Labrador boundary at the western end of OSNAP west	**0.53**
	Labrador boundary at the eastern end of OSNAP west	−0.23
	52°N west boundary	**0.47**
	46°N west boundary	**0.33**

Note. The regional density is separated into a boundary or interior regions, where the boundary region extends from the coast to the 2,000 m isobath. Values of at least 99% confidence of magnitude of 0.44 are in bold and of 98% confidence of magnitude of 0.32 in italics.

the western boundary. This mismatch with our data-based reconstruction is likely due to the timescale of interest as we are using annual means and the OSNAP record to date is dominated by sub-seasonal variability. Similar to our study, Menary et al. (2020) obtained a correlation of 0.6 using annual model data between the overturning for the eastern side of the basin and the density along the western side of the Irminger Sea.

The overturning for OSNAP west is strongly correlated with the density above the $\sigma = 27.7$ surface around the Labrador Sea (reaching 0.62 at zero lag when including both end points of OSNAP west in Table 3). The correlations reduce when including only a single end point of OSNAP west (Table 3), consistent with the analysis of Li et al. (2021) for 4 years of monthly OSNAP data.

Maps of the correlation between the time series for the overturning for OSNAP west and the density above the 27.7 surface reveal high correlations along the western side of the Labrador Sea; a similar pattern occurs for the meridional overturning across the western side of 60°N (Figures 6c and 6d). The meridional overturning for 52°N and 40°N shows similar correlation patterns to that of OSNAP west, revealing a positive correlation to the western boundary density (Figures 6e and 6f).

2.6. Causality in the Connections Between the Regional Density and Overturning

Understanding the causes of the correlations between regional density changes and the overturning, especially in remote regions, needs further investigation. There may be a direct causal relationship when the local atmospheric forcing induces a boundary density anomaly, which then generates an overturning response. However, positive correlations between regional density changes in one region (such as the Irminger Sea) and overturning over a wider region (such as the eastern basin) may arise because:

1. The local boundary density changes may be influenced by upstream density changes, which are communicated downstream, and the upstream density changes provide the actual control of the overturning;
2. The local boundary density changes may be forced by a large-scale atmospheric variability that also forces boundary density, and hence overturning, changes elsewhere.

To gain insight into these possible connections, lagged correlations are evaluated for three different combinations of time series of the regional densities, which are either upstream or downstream of the Irminger Sea and the Labrador Sea. First, considering the boundary density for the Irminger Sea (defined by a shoreward region ranging from 0 to 2,000 m in depth, Figure 2) and the upstream regional density anomaly in the Iceland Basin, there is

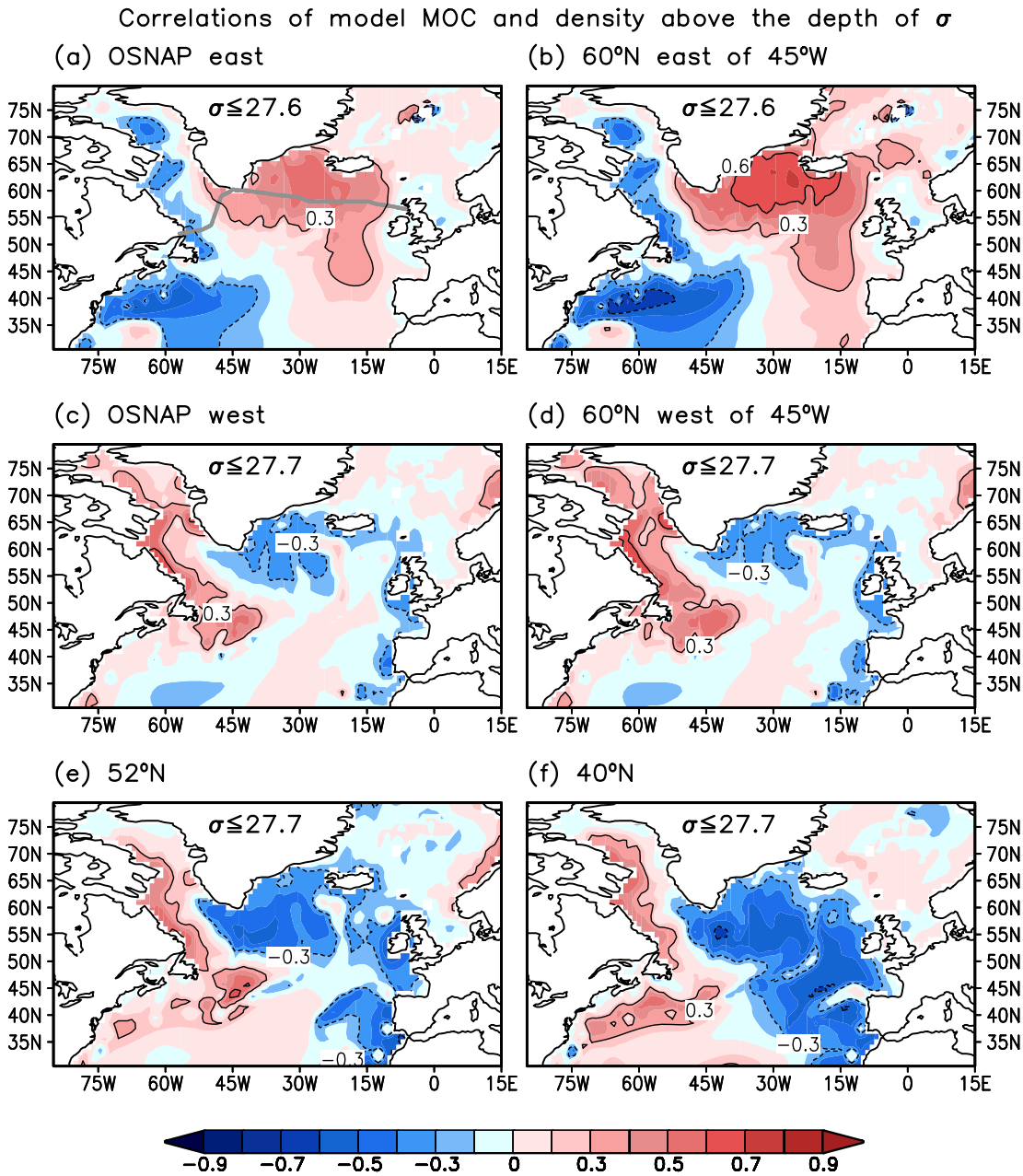

Figure 6. Historical data-based correlations between the thickness-weighted average density above a potential density surface σ and different time series of the overturning from 1960 to 2020: (a) overturning for OSNAP east and (b) meridional overturning for 60°N east of 45°W, both relative to the 27.6 surface; (c) overturning for OSNAP west, (d) meridional overturning for 60°N west of 45°W, (e) meridional overturning for 52°N, and (f) meridional overturning for 40°N, all both relative to the 27.7 surface.

a strong correlation at zero lag of 0.86 (Figure 7a). Both density anomalies are probably responding to the same large-scale pattern in atmospheric forcing although there is a possibility of a rapid communication in less than a year between each region.

Second, for the boundary density anomalies of the Irminger Sea and the Labrador Sea, the changes in the Irminger Sea precede the changes in the Labrador Sea with a maximum correlation of 0.7 with a 3-year lag (Figure 7b). This response is consistent with the boundary density in the Irminger Sea being advected along the boundary to the Labrador Sea as well as consistent with the recent modeling study of Menary et al. (2020). This response is

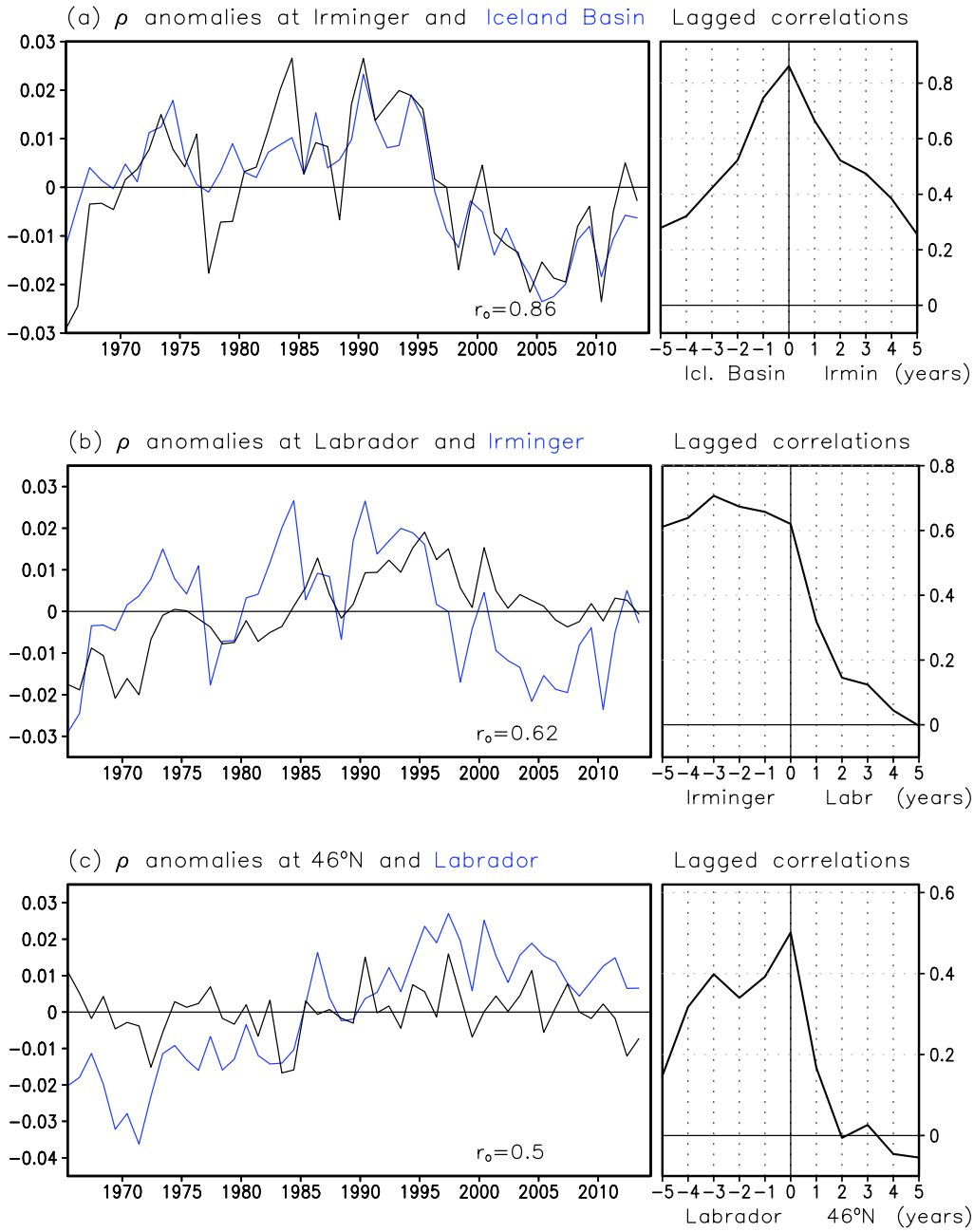

Figure 7. Time series of regional density anomalies together with their lagged correlations (with r_o being the zero lag correlation): (a) Iceland Basin (blue) and the shallow Irminger Sea (depths 0–2,000 m, black) and with the upstream Iceland Basin lagged; (b) The Labrador Sea (black) and the shallow Irminger Sea (depths 0–2,000 m) (blue), with the Irminger Sea lagged (so a maximum correlation at −3 years implies that the Irminger Sea response occurs before the Labrador Sea response); (c) The shallow Labrador Sea and west 46°N (both for depths 0–2,000 m) (black) with the Labrador Sea lagged.

also consistent with the overturning for OSNAP east not being significantly correlated with the density changes in the Labrador Sea at zero lag (Table 3).

Finally, for the boundary density changes of the Labrador Sea and further south on the western boundary of the subpolar gyre at 46°N, there is a maximum correlation of 0.5 at zero lag together with a correlation of 0.4 at 3 years lag (Figure 7c). This signal may then be due to a combination of a density response at zero lag to coherent changes in atmospheric forcing together with a downstream communication of the Labrador Sea density signals on a timescale of 3 years. Hence, the overturning for OSNAP west correlates with the boundary density changes

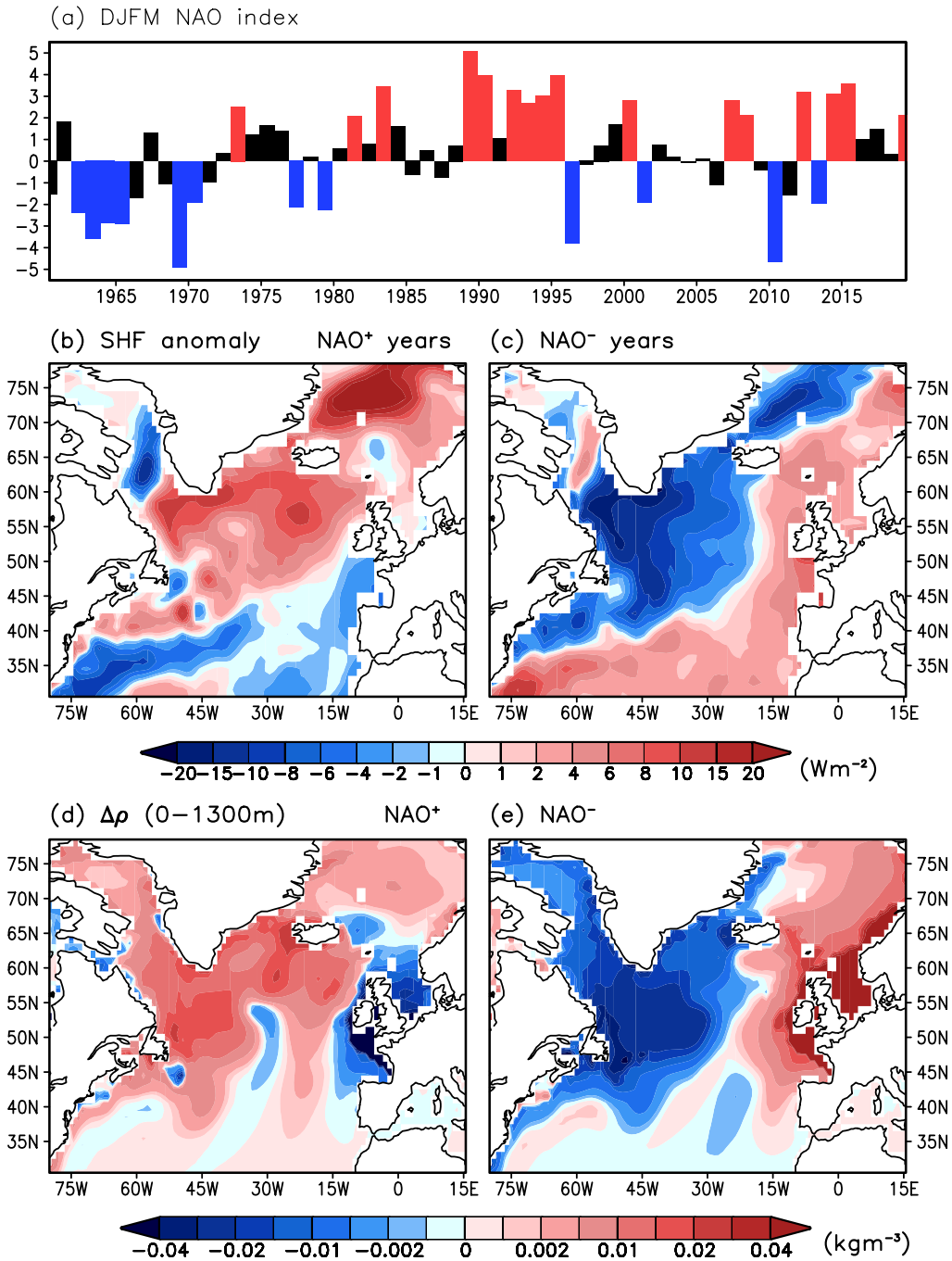

Figure 8. (a) Winter NAO index based on December to March. The time record is separated into characteristic periods for NAO+ (red) and NAO− (blue) years; (b) NAO+ and (c) NAO− surface heat flux (SHF) anomalies from the ocean to the atmosphere for European Centre for Medium-Range Weather Forecasts (ECMWF) for the years defined from (a); (d) NAO+ and (e) NAO− upper ocean density changes after 5 years of sustained NAO anomalies from only the surface heat flux.

for the Labrador Sea and the meridional overturning at lower latitudes (Table 3), involving the combined effects of coherent atmospheric forcing and boundary communication of density anomalies.

Unraveling these competing effects of a local response to large-scale coherent patterns of atmospheric forcing and a communication and transport of density anomalies is challenging using the data-based reconstructions. Consequently, a series of forward model experiments (Section 3) are used next to reveal how regional density anomalies are formed and spread over the subpolar basin and how they connect to the overturning changes on the

western and eastern sides of the basin, including whether those overturning changes on each side of the basin are reinforcing or opposing each other.

3. Forward-Model Experiments for the Overturning Response

The aim is now to assess how regional density changes connect to the overturning changes across the subpolar basin and to separate the effects of local versus upstream responses to atmospheric forcing.

3.1. Methods

Forward model experiments are conducted using the global MIT general circulation model (Marshall et al., 1997) with a 1° grid with 23 vertical levels over the globe. The model is initialized from the climatological temperatures and salinities and forced by the climatological monthly mean surface heat fluxes and wind stress from ECMWF reanalyzes. In order to reduce the model drift, the sea-surface temperature (SST) is relaxed to the climatological monthly mean SST on a timescale of 15 days during the first 50 years of the spin-up. The virtual heat fluxes from the restoring term are diagnosed on a monthly basis and combined with the surface heat fluxes. This combined forcing is used for the rest of the spin-up with the SST relaxation switched off. Due to the larger uncertainties in the freshwater fluxes, the use of explicit fluxes is avoided and the sea-surface salinity is relaxed to the climatological monthly mean sea-surface salinity on a timescale of 15 days. Monthly mean regional surface forcing anomalies are applied for a period of 10 years after the initial 100 years spin-up. The regional forcing experiments employ surface forcing appropriate for different composite states of the NAO (Figure 8a) based on station data (Hurrell, 2013), consisting of 16 years for NAO+ and 12 years for NAO−. The model diagnostics are presented in terms of the difference between the model experiment using the modified forcing and a model control using climatological forcing, which minimizes the effects of potential model drift. The modified forcing is taken from atmospheric reanalyzes by ECMWF for the appropriate years using ERA40 for 1960–1978 and ERA Interim for 1979–2020. The forward model experiments do not include any internal relaxation to the historical data, so do contain model drift and systematic errors, such as including greater convection in the Labrador Sea and larger changes in the overturning in OSNAP west than that revealed in the data-based reconstructions.

The MOC along the OSNAP line from the forward control run is 15.7 Sv for OSNAP east and 7.0 Sv for OSNAP west. The overturning for OSNAP east is in reasonable agreement with the data-based reconstructions of 16.49 ± 0.62 Sv (Table 1). However, the overturning for OSNAP west is larger than the data-based estimate of 3.42 ± 0.41 Sv. This larger value is typical for coarse-resolution models that are unconstrained by observations, which may be due to overestimating deep convection in the Labrador Sea and resulting changes in density distribution.

The modifications in the annual surface heat flux associated with the winter NAO typically reach ±20 Wm^{-2}, providing enhanced cooling over much of the western subpolar gyre during NAO+ and less cooling during NAO− (Figures 8b and 8c). The large-scale coherence in the surface cooling anomaly for NAO+ leads to an increase in the density for the upper 1,300 m over much of the subpolar gyre, particularly over the Labrador Sea, the Irminger Sea, and the Iceland Basin (Figure 8d). The surface warming anomaly for NAO− instead leads to a lightening over the western side of the subpolar gyre, particularly over the Labrador Sea and the Irminger Sea (Figure 8e).

For these forward experiments, the combined effect of changes in surface winds and surface heat fluxes linked to a NAO+ state leads to a strengthening in the overturning by 0.73 Sv for OSNAP west and 2.6 Sv for OSNAP east, while a NAO− state leads to a weakening in the overturning by −3.65 Sv for OSNAP west and −1.97 Sv for OSNAP east (Table 4). These overturning changes are the same sign as those diagnosed from the data-based reconstructions (Table 1), which for NAO+ state reach 0.44 Sv for OSNAP west and 1.12 Sv for OSNAP east, and for NAO− state reach −0.16 Sv for OSNAP west and −0.39 Sv for OSNAP east. Hence, for different states of the NAO, the overturning contributions have the same sign on both the western and eastern sides of the basin; this similarity in sign occurs in both our diagnostics of the data-based reconstructions and these forward model experiments when the forcing is applied to the entire basin.

This response is primarily controlled by the effects of the surface heat fluxes since there are similar large responses if anomalous surface heat fluxes are imposed together with climatological winds: the overturning

Table 4
Forward Model Experiments for Overturning Changes (Sv) Across OSNAP Line After 5 Years of Subsampled NAO ± Forcing From ECMWF, Which Is Either Includes Anomalous Wind or Buoyancy Forcing or Combined Anomalies in Wind and Buoyancy Forcing

	NAO+		NAO−	
Forcing over entire domain	OSNAP west	OSNAP east	OSNAP west	OSNAP east
NAO winds	0.02	0.36	−0.19	−0.48
NAO buoyancy forcing	1.01	1.97	−3.44	−1.58
NAO winds + buoyancy forcing	0.73	2.60	−3.65	−1.97
Overturning change from historical data for $\sigma_{max} = 27.7$	0.44	1.12	−0.16	−0.39

Note. Overturning is defined relative to the same maximum density limit, $\sigma_{max} = 27.8$, across the entire OSNAP line, so that the overturning across the full line is the sum of the OSNAP west and east contributions. In addition, the overturning change is included for the historical data analysis (Table 1) for selected NAO+ and NAO− periods (Figure 8a) with a lighter fixed density limit of $\sigma_{max} = 27.7$.

increases by 1.01 Sv for OSNAP west and 1.97 Sv for OSNAP east, respectively, while the equivalent anomalous surface forcing for NAO− leads to a reduction in the overturning by −3.44 Sv for OSNAP west and −1.58 Sv for OSNAP east (Table 4). This stronger response for OSNAP west to NAO− forcing is due to larger anomalies in the surface heat flux in the western basin as the overturning responses are similar in magnitude if the surface forcing anomaly is replaced by a spatially uniform ± 10 Wm^{-2} (not shown). The overturning responses are in accord with the sign of the densification or lightening for NAO+ and NAO− states (Figures 8d and 8e). In contrast, there are much weaker responses if the surface forcing includes anomalous winds and climatological surface heat fluxes: the overturning only strengthens for NAO+ by 0.02 Sv for OSNAP west and 0.36 Sv for OSNAP east, while the overturning only weakens for NAO− by −0.19 Sv for OSNAP west and −0.48 Sv for OSNAP east. Hence, the buoyancy forcing is key to the pronounced changes in the subpolar overturning in our model experiments.

3.2. Overturning, Density, and Circulation Responses to Localized Regional Forcing

Our aim is now to identify the effects of localized buoyancy forcing in controlling the overturning responses, so separating out the effect of a local response to density changes versus either far-field density responses and/or the response to large-scale coherent patterns in atmospheric forcing. The subpolar domain is separated into seven individual regions, including the Labrador Sea, the Irminger Sea, and the Iceland Basin (Figure 2). Separate modeling experiments are then performed where the NAO+ or NAO− surface buoyancy forcing is applied only to an individual region (Table 5). This process is repeated for each of the seven individual regions, so that the response to the buoyancy forcing over the entire domain may be viewed in terms of a summation of the individual responses to the regional forcing.

For OSNAP west, the localized forcing for NAO+ and NAO− over the Labrador Sea and the Irminger Sea provides the dominant contribution to the overturning, accounting for 0.88 and 0.59 Sv for NAO+ versus −2.21 Sv and −0.98 Sv for NAO−, respectively (Table 5).

For OSNAP east, the localized forcing over a broader region provides comparable contributions to the change in the overturning: the forcing for NAO+ over the Irminger Sea, the Iceland Basin, and the southeast subpolar gyre account for 0.49 Sv, 0.81 Sv, and 0.38 Sv, respectively; while the forcing for NAO− over the Irminger Sea, the Iceland Basin, the southwest, and southeast subpolar gyre account for −0.54 Sv, −0.31 Sv, −0.33 Sv, and −0.39 Sv, respectively (Table 5).

There are contrasting responses in terms of whether the overturning changes reinforce each other or oppose each other over the subpolar basin. For the Labrador Sea regional forcing case, the overturning response for OSNAP east is weak and the opposing sign of that for OSNAP west, while instead for the Irminger Sea regional forcing case, there are reinforcing contributions for OSNAP west and east. In order to understand these different responses, consider snapshots of the regional density response at years 1, 5, and 10 after sustained patterns of the buoyancy forcing are applied after 100 years of initial spin-up (Figure 9 with the anomalous forcing contained within the gray contour).

Table 5
Forward Model Regional Experiments Showing the Overturning Changes (Sv) After 5-Year Response to Anomalous Buoyancy Forcing, Where the Forcing Is Either Only Applied to Selected Individual Regions or for All of the Regions Combined Together

	NAO+		NAO−	
Buoyancy forcing only over regional domain	OSNAP west	OSNAP east	OSNAP west	OSNAP east
Labrador Sea (LS)	0.88	−0.03	−2.21	0.04
Irminger Sea (IS)	0.59	0.49	−0.98	−0.54
Iceland Basin (IB)	−0.01	0.81	−0.12	−0.31
Southwest subpolar gyre (SW)	0.32	0.10	−0.69	−0.33
Southeast subpolar gyre (SE)	−0.11	0.38	−0.09	−0.39
European shelf (ES)	0.0	0.04	0.0	−0.15
Northeast and Norwegian Sea (NE)	0.01	0.06	−0.04	−0.01
All of the above forcing applied together	1.68	1.85	−4.13	−1.69

Note. The different regions are defined in Figure 2. The buoyancy forcing is regionally subsampled for NAO± composite states based upon 16 years of NAO+ and 12 years of NAO− using a magnitude threshold of 1.8 with station data (Figure 8a, red and blue) from ECMWF. Overturning is defined relative to the same density surface, σ_{max} = 27.8, across the entire OSNAP line, so that the overturning across the full line is the sum of the OSNAP west and east contributions.

For enhanced surface cooling for NAO+ applied only over the Labrador Sea, a positive density anomaly forms over the forcing region, which then spreads into the subpolar gyre and along the western boundary (Figure 9, left panel). After 5 years, there is a dipole and a lighter anomaly is formed to the east of the dense anomaly. Crucially, there are opposing signs in the boundary density anomalies in the Labrador Sea and the Irminger Sea, which are consistent with there being opposing sign contributions for the overturning changes for OSNAP west and east (Table 5). There are similar responses with the opposing sign for NAO− (not shown).

For enhanced surface cooling for NAO+ applied only over the Irminger Sea, a positive density anomaly again forms over the forcing region, which then spreads along the western boundary into the Labrador Sea (Figure 9, right panel). After 5–10 years, there is again a dipole with a lighter anomaly to the southeast of the dense anomaly. Crucially, there are similar signs in the boundary density anomalies in the Labrador Sea and the Irminger Sea, which are consistent with there being reinforcing sign contributions for the overturning changes across OSNAP west and east (Table 5). There are similar responses with the opposing sign for NAO− (not shown).

The dipole of positive and negative density anomalies is created through the effect of the direct forcing and the resulting adjustment of the overturning circulation and horizontal transport (Figure 10). For a formation of denser fluid in the Labrador Sea (Figure 9, left panel), there is a strengthening in the overturning and meridional heat transport (Figure 10a, left panel), enhancing the influx of warmer, lighter waters into the northwestern part of the subpolar gyre, and reducing the strength of the boundary transport from the Irminger Sea to the Labrador Sea, and the transport from the Nordic Seas to the Irminger Sea (Figure 10a, right panel). Hence, the dense anomaly formed in the Labrador Sea is accompanied by a lighter boundary density anomaly formed in the Irminger Sea. This dipole in boundary density is consistent with the opposing sign contributions for the overturning changes for OSNAP west and east obtained in this experiment with only local density forcing in the Labrador Sea (Table 5).

For the Irminger Sea case, the localized forcing associated with the NAO+ state leads to an increase in the boundary density in the Irminger Sea and downstream similar changes in the Labrador Sea (Figure 9, right panel). There is an adjustment to the circulation involving a strengthening in the overturning again (Figure 10b, left panel), but now the local density forcing leads to a strengthening in the transport from the Nordic Seas to the Irminger Sea and from the Irminger Sea to the Labrador Sea (Figure 10b, right panel). The similar signs in the boundary density changes in the Labrador Sea and the Irminger Sea are consistent with the similarly signed contributions for the overturning changes for OSNAP west and east.

Hence, the regional experiments suggest that a local forcing over the Labrador Sea does not provide the similarly signed overturning responses over the western and eastern sides of the subpolar basin, while the regional forced

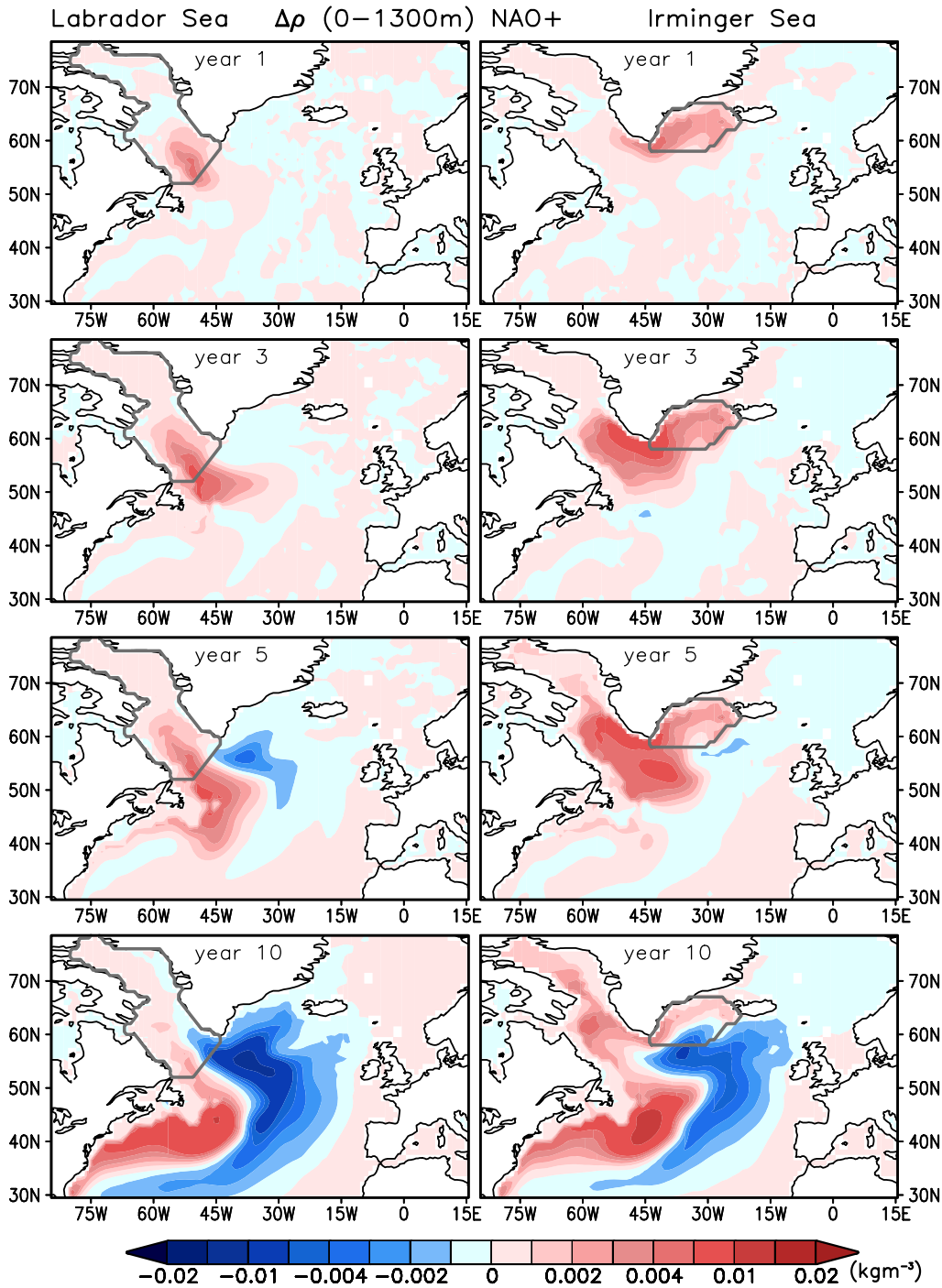

Figure 9. Regional experiments where NAO+ forcing is only applied for the Labrador Sea (left panel) or the Irminger Sea (right panel) using monthly mean surface heat anomalies from European Centre for Medium-Range Weather Forecasts (ECMWF) subsampled NAO+. Density changes are shown after 1, 3, 5, and 10 years (after an initial spin-up of 100 years).

experiments over the Irminger Sea provide overturning responses consistent with the data-based reconstructions and the basin-wide forcing experiments (Tables 1, 4, and 5).

Given that there is a large-scale coherence to the atmospheric forcing of the subpolar basin, these regional experiments offer a cautionary note as to how basin-wide model experiments may be interpreted. The Labrador Sea density provides a useful metric for the overturning over the western side of the subpolar basin and at lower

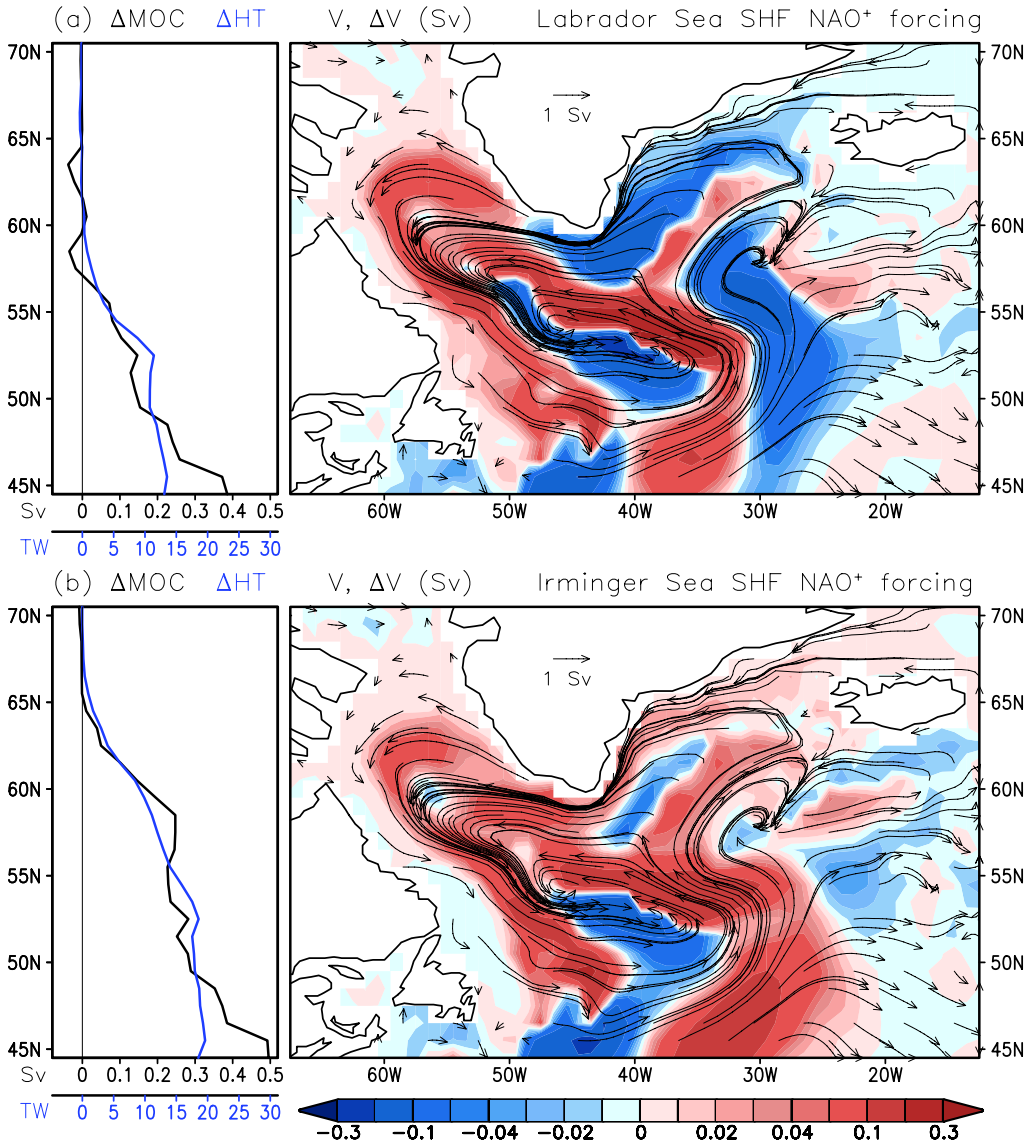

Figure 10. Change in the meridional overturning circulation (MOC, Sv, black) and the northward heat transport (HT, TW, blue) relative to the control run with latitude (left panel) for 10 years of NAO+ surface heat flux (SHF) forcing localized in (a) the Labrador Sea or (b) the Irminger Sea. In the right panels, the corresponding horizontal transport patterns over the upper 1,300 m for NAO+ are denoted by the vectors (black, Sv) together with changes in the strength of the horizontal transport for NAO+ minus the control (colors). For both cases, the density forcing increases the meridional overturning and enhances the northward heat transport (left panels), so acting to lighten the upper ocean. In panel (a), an increase in the density in the Labrador Sea with NAO+ forcing is associated with a strengthening in northwestern subpolar circulation enhancing the influx of warmer, lighter waters as well as a reduced horizontal transport along the boundary from the Irminger Sea to the Labrador Sea. Conversely, in panel (b), an increase in the density in the Irminger Sea with NAO+ forcing is associated with a strengthening in the boundary transport from the Irminger Sea to the Labrador Sea as well as from the Nordic Seas into the Irminger Sea.

latitudes over the basin as has been widely exploited in model studies (Delworth et al., 1993; Eden & Willebrand, 2001) and inferences from regional density changes (Robson et al., 2016). However, in our regional experiments, a local forcing over the Labrador Sea acts to decrease the overturning over the eastern side of the basin. Consequently, the Irminger Sea density provides a more reliable metric of the overturning changes for the eastern basin.

4. Discussion

The relationship between the overturning of the subpolar North Atlantic and regional density is assessed using a combination of historical, data-based reconstructions of the overturning over the last 60 years and forward model regional experiments using buoyancy and wind forcing, characteristic of different states of the NAO.

The data-based reconstructions are in accord with the OSNAP measurements of the subpolar overturning defined in density coordinates, which are dominated by an eastern basin contribution between Greenland and Scotland (Li et al., 2021; Lozier et al., 2019). The stronger overturning contribution for the eastern side of the basin is consistent with the larger west-east boundary density contrast between Greenland and Scotland compared with the weaker overturning contribution and boundary density contrast from the western side of the Labrador Sea to the southern tip of Greenland. In our reconstructions, the overturning for the eastern side of the basin is strongly correlated with density changes over the Irminger Seas, while the overturning for the western side of the basin is only strongly correlated with boundary density changes on the southwestern shelf of the Labrador Sea and the southern tip of Greenland. In these density coordinates, the zonally integrated geostrophic velocity along potential density surfaces may be estimated from boundary contrasts in Montgomery potential, which are determined by a combination of the density and sea surface height distributions.

There are caveats in the accuracy of the data-based reconstructions of the density with the uncertainty in the density larger than the actual anomalies (Hodson et al., 2014) and differences in the magnitude of density metrics according to the data source (Robson, Sutton, & Smith, 2014). These differences in density reconstruction then lead to resulting differences in the reconstruction of the geostrophic component of the overturning as revealed in a comparison of 6 different data-based ocean analyses including the same Hadley Center product as used here (Karspek et al., 2015). While accepting these caveats, skillful prediction of the overturning circulation in the North Atlantic basin still requires the inclusion of these data-constrained ocean reanalysis products for initialization (Matei et al., 2012; Robson et al., 2012; Robson, Sutton, & Smith, 2014; Yeager & Danabasoglu, 2014).

To gain some insight into causal connections between the overturning and the regional density changes, a suite of forward model experiments are conducted to separate out the effect of local and far-field responses to the atmospheric forcing. The model experiments include anomalous atmospheric forcing for NAO+ and NAO− states, but the anomalous forcing is only applied to a selected region, then this process is repeated for 7 different regions making up the subpolar basin. In these experiments, a localized density increase over the Irminger Sea increases the overturning over both the western and eastern sides of the basin due to dense waters spreading to the Labrador Sea. This response is consistent with the Menary et al. (2020) interpretation of Labrador Sea density changing due to upstream forcing in the Irminger Sea. Conversely, a localized density increase over the Labrador Sea increases the overturning on the western side of the basin, but decreases the overturning on the eastern side of the basin due to a greater influx of warmer, lighter waters. These regionally forced experiments then reveal that forcing over the Irminger Sea leads to reinforcing western and eastern basin contributions to the overturning, which are consistent with our data-based diagnostics of how the subpolar overturning responds to the NAO+ or NAO− forcing. In contrast, the regional forcing experiments for the Labrador Sea lead only to an increase in the overturning for the western basin.

Hence, the Irminger Sea density provides a useful metric for revealing whether there are likely to be reinforcing overturning changes in the western and eastern sides of the subpolar basin, while the Labrador Sea density provides a useful metric for the overturning for the western basin and lower latitudes of the subpolar gyre. However, caution needs to be applied in interpreting any implied causality in these relationships involving the Labrador Sea density and the overturning for the eastern basin since this connection is partly due to the coherent pattern of atmospheric forcing driving similarly signed density changes over much of the basin and partly due to a communication and transport of density anomalies, connecting upstream forcing to downstream responses.

Appendix A: Historical Data-Based Model Reconstructions of the Overturning in Density Space

The data-based reconstructions of the overturning are also evaluated relative to a constant maximum density, $\sigma_{max} = 27.7$ surface in Equation 1 (Figure A1). For this definition, overturning across the full line equals the sum of the overturning across the western section and the overturning across the eastern section. The overturning

across each individual section is less than or equal to the OSNAP definition of the maximum overturning crossing the section.

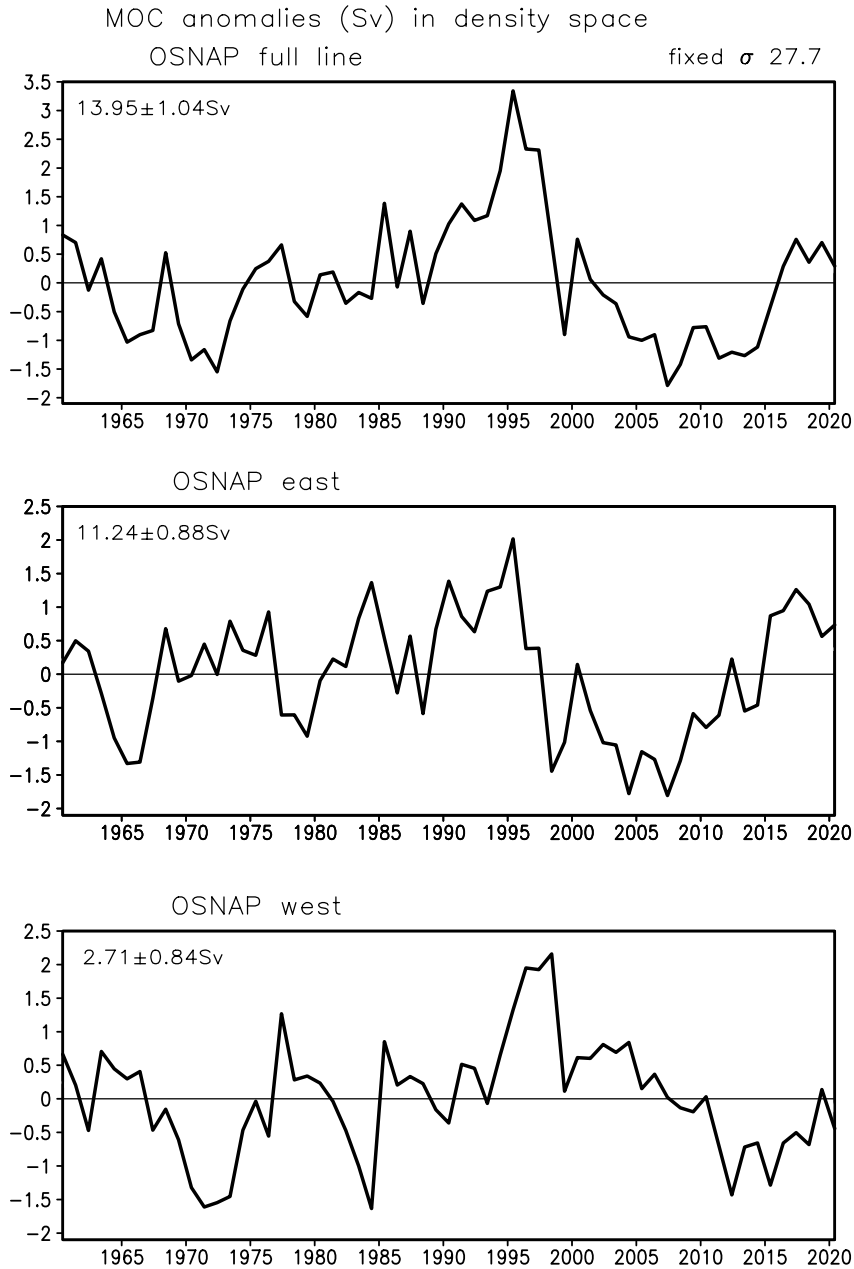

Figure A1. Historical data-based model reconstructions of the overturning in density space (Sv) across the OSNAP full line from 1960 to 2020: (a) for the full line, (b) east of 45°W, and (c) west of 45°W. Numbers show the long-term averages and standard deviations based on annual values. The overturning estimates are always defined relative to the same maximum density σ_{max} = 27.7 surface in Equation 1. For this definition, overturning across the full line = the overturning across the western section + overturning across the eastern section.

The data-based reconstructions reveal subtropical and subpolar gyre circulations over the basin with sea surface height changes reaching +50 cm over the subtropics and −110 cm in the subpolar gyre in the climate mean from 1960 to 2020 (Figure A2a). The pattern in the double gyre circulation is enhanced during a NAO+ composite with sea surface height anomalies reaching magnitudes of 4 cm (Figure A2b) and conversely weakened for a NAO− composite (Figure A2c).

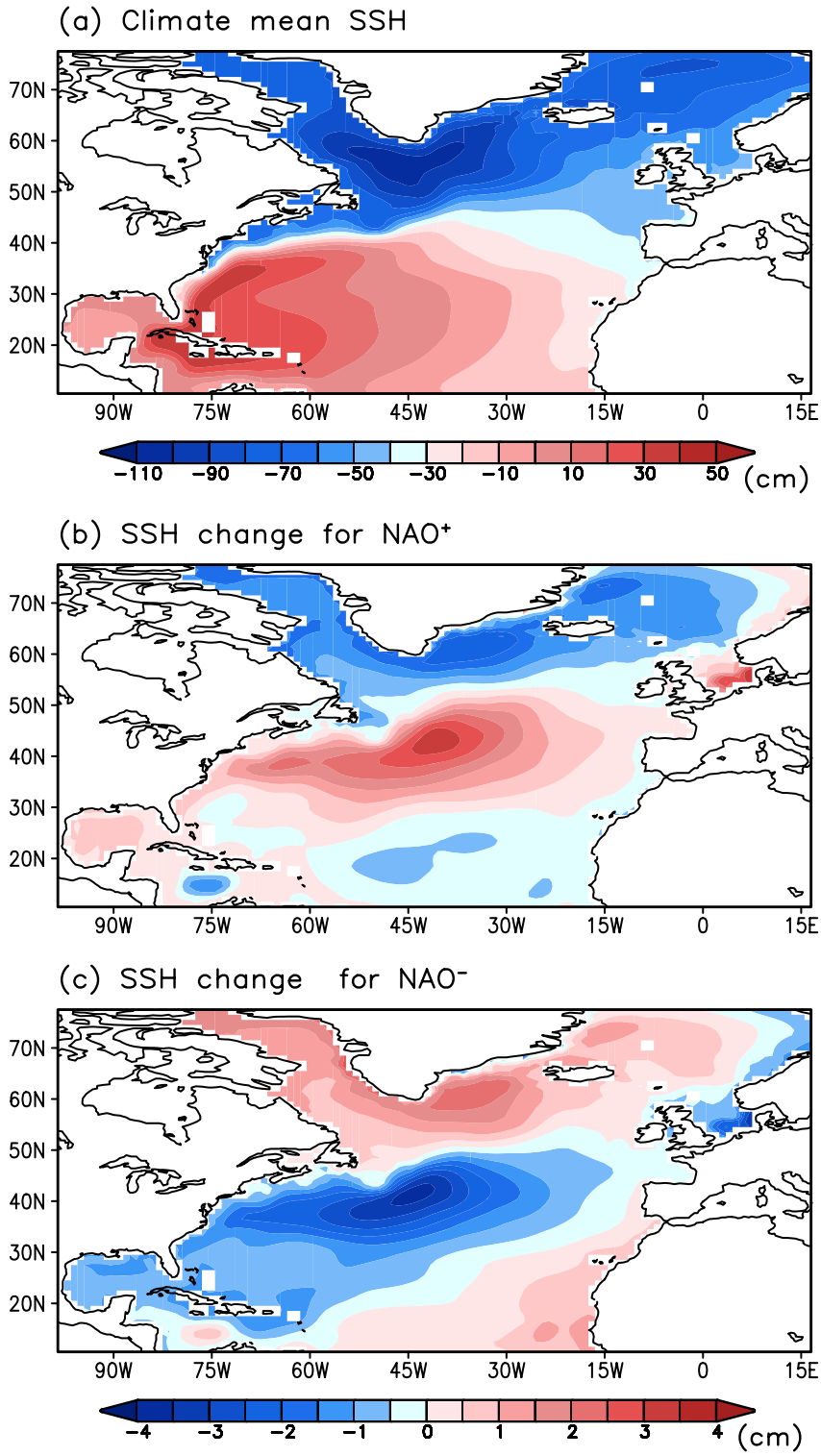

Figure A2. Data-based reconstructions for the annual mean sea surface height (cm): (a) climate mean from 1960 to 2020, (b) NAO+ composite, and (c) NAO− composite.

Data Availability Statement

The OSNAP array data from years 2014 to 2018 are available at http://hdl.handle.net/1853/63707 and www.o-snap.org. The annual mean temperature and salinity data from 1960 to 2020 from the Met Office statistical ocean reanalysis (Smith et al., 2015) and our data-based reconstructions of the meridional overturning circulation in density space along the OSNAP line, OSNAP west, and OSNAP east are available at https://doi.org/10.5281/zenodo.6524716.

Acknowledgments
VR and RGW acknowledge support from the UK Natural Environment Research Council NE/K010972/1 and NE/T013494/1. MSL acknowledges the support from the Physical Oceanography Program of the National Science Foundation via Grant OCE-17-56223. NPH was supported by UK Natural Environment Research Council National Capability program CLASS (NE/R015953/1), and NERC grants UK OSNAP (NE/K010875/1 and NE/K010875/2) and UK OSNAP Decade (NE/T00858X/1). We thank Feili Li for advice as to the correlations for the OSNAP time series. DS was supported by the Met Office Hadley Centre Climate Programme funded by BEIS and Defra. We thank four referees for constructive comments that strengthened the study.

References

Baehr, J., Hirschi, J., Beismann, J. O., & Marotzke, J. (2004). Monitoring the meridional overturning circulation in the North Atlantic: A model-based array design study. *Journal of Marine Research*, *62*(3), 283–312. https://doi.org/10.1357/0022240041446191

Bingham, R. J., Hughes, C. W., Roussenov, V., & Williams, R. G. (2007). Meridional coherence of the North Atlantic meridional overturning circulation. *Geophysical Research Letters*, *34*(23). https://doi.org/10.1029/2007gl031731

Bleck, R., & Smith, L. T. (1990). A wind-driven isopycnic coordinate model of the north and equatorial Atlantic Ocean: 1. Model development and supporting experiments. *Journal of Geophysical Research*, *95*(C3), 3273–3285. https://doi.org/10.1029/jc095ic03p03273

Buckley, M. W., & Marshall, J. (2016). Observations, inferences, and mechanisms of Atlantic Meridional overturning circulation variability: A review. *Reviews of Geophysics*, *54*(1), 5–63. https://doi.org/10.1002/2015RG000493

Delworth, T., Manabe, S., & Stouffer, R. J. (1993). Interdecadal variations of the thermohaline circulation in a coupled ocean-atmosphere model. *Journal of Climate*, *6*(11), 1993–2011. https://doi.org/10.1175/1520-0442(1993)006<1993:ivottc>2.0.co;2

Eden, C., & Willebrand, J. (2001). Mechanism of interannual to decadal variability of the North Atlantic circulation. *Journal of Climate*, *14*(10), 2266–2280. https://doi.org/10.1175/1520-0442(2001)014<2266:moitdv>2.0.co;2

Foukal, N. P., & Lozier, M. S. (2016). On the propagation of sea-surface temperature anomalies from the subtropical gyre to the subpolar gyre in the North Atlantic. *Nature Communications*, *7*(1), 11333. https://doi.org/10.1038/ncomms11333

Gent, P. R., & McWilliams, J. C. (1990). Isopycnal mixing in ocean circulation models. *Journal of Physical Oceanography*, *20*(1), 150–155. https://doi.org/10.1175/1520-0485(1990)020<0150:imiocm>2.0.co;2

Greatbatch, R. J., Fanning, A. F., Goulding, A. D., & Levitus, S. (1991). A diagnosis of interpentadal circulation changes in the North Atlantic. *Journal of Geophysical Research*, *96*(C12), 22009–22023. https://doi.org/10.1029/91JC02423

Hirschi, J., & Marotzke, J. (2007). Reconstructing the meridional overturning circulation from boundary densities and the zonal wind stress. *Journal of Physical Oceanography*, *37*(3), 743–763. https://doi.org/10.1175/jpo3019.1

Hodson, D. L. R., Robson, J. I., & Sutton, R. T. (2014). An anatomy of the cooling of the North Atlantic Ocean in the 1960s and 1970s. *Journal of Climate*, *27*(21), 8229–8243. https://doi.org/10.1175/JCLI-D-14-00301.1

Holliday, N. P., Bacon, S., Cunningham, S. A., Gary, S. F., Karstensen, J., King, B. A., et al. (2018). Subpolar North Atlantic overturning and gyre-scale circulation in the summers of 2014 and 2016. *Journal of Geophysical Research: Oceans*, *123*(7), 4538–4559. https://doi.org/10.1029/2018jc013841

Hurrell, J. (2013). *The climate data guide: Hurrell North Atlantic Oscillation (NAO) index (Station-Based)*. The National Center for Atmospheric Research Staff.

Karspeck, A. R., Stammer, D., Kohl, A., Danabasoglu, G., Balmaseda, M., Smith, D. M., et al. (2015). Comparison of the Atlantic meridional overturning circulation between 1960 and 2007 in six ocean reanalysis products. *Climate Dynamics*, *49*(3), 957–982. https://doi.org/10.1007/s00382-015-2787-7

Li, F., Lozier, M. S., Bacon, S., Bower, A. S., Cunningham, S. A., de Jong, M. F., et al. (2021). Subpolar North Atlantic western boundary density anomalies and the meridional overturning circulation. *Nature Communications*, *12*(1), 1–9. https://doi.org/10.1038/s41467-021-23350-2

Li, F., Lozier, M. S., Danabasoglu, G., Holliday, N. P., Kwon, Y.-O., Romanou, A., et al. (2019). Local and downstream relationships between Labrador Sea Water volume and North Atlantic meridional overturning circulation variability. *Journal of Climate*, *32*(13), 3883–3898. https://doi.org/10.1175/jcli-d-18-0735.1

Li, F., Lozier, M. S., & Johns, W. E. (2017). Calculating the meridional volume, heat, and freshwater transports from an observing system in the subpolar North Atlantic: Observing system simulation experiment. *Journal of Atmospheric and Oceanic Technology*, *34*(7), 1483–1500. https://doi.org/10.1175/jtech-d-16-0247.1

Lozier, M. S., Bacon, S., Bower, A. S., Cunningham, S. A., De Jong, M. F., De Steur, L., et al. (2017). Overturning in the subpolar North Atlantic program: A new international ocean observing system. *Bulletin of the American Meteorological Society*, *98*(4), 737–752. https://doi.org/10.1175/bams-d-16-0057.1

Lozier, M. S., Li, F., Bacon, S., Bahr, F., Bower, A. S., Cunningham, S. A., et al. (2019). A sea change in our view of overturning in the subpolar North Atlantic. *Science*, *363*(6426), 516–521. https://doi.org/10.1126/science.aau6592

Lozier, M. S., Roussenov, V., Reed, M. S. C., & Williams, R. G. (2010). Opposing decadal changes for the North Atlantic meridional overturning circulation. *Nature Geoscience*, *3*(10), 728–734. https://doi.org/10.1038/ngeo947

Marotzke, J., Giering, R., Zhang, K. Q., Stammer, D., Hill, C., & Lee, T. (1999). Construction of the adjoint MIT ocean general circulation model and application to Atlantic heat transport sensitivity. *Journal of Geophysical Research*, *104*(C12), 29529–29547. https://doi.org/10.1029/1999jc900236

Marshall, J., Hill, C., Perelman, L., & Adcroft, A. (1997). Hydrostatic, quasi-hydrostatic, and nonhydrostatic ocean modeling. *Journal of Geophysical Research*, *102*(C3), 5733–5752. https://doi.org/10.1029/96JC02776

Matei, D., Pohnmann, H., Jungclas, J., Müller, W., Haak, H., & Marotzke, J. (2012). Two tales of initializing decadal climate prediction experiments with the ECHAM5/MPI-OM model. *Journal of Climate*, *25*(24), 8502–8522. https://doi.org/10.1175/jcli-d-11-00633.1

McCarthy, G. D., Brown, P. J., Flagg, C. N., Goni, G., Houpert, L., Hughes, C. W., et al. (2020). Sustainable observations of the AMOC: Methodology and technology. *Reviews of Geophysics*, *58*(1), e2019RG000654. https://doi.org/10.1029/2019rg000654

McDougall, T. J., Feistel, R., Millero, F. J., Jackett, D. R., Wright, D. G., King, B. A., et al. (2009). The international thermodynamic equation of seawater 2010 (TEOS-10): Calculation and use of thermodynamic properties. *Global Ship-Based Repeat Hydrography Manual, IOCCP Report No. 14*.

McDougall, T. J., & Klocker, A. (2010). An approximate geostrophic streamfunction for use in density surfaces. *Ocean Modelling*, *32*(3–4), 105–117. https://doi.org/10.1016/j.ocemod.2009.10.006

Mellor, G. L., Mechoso, C. R., & Keto, E. (1982). A diagnostic calculation of the general circulation of the Atlantic Ocean. *Deep-Sea Research Part A. Oceanographic Research Papers*, *29*(10), 1171–1192. https://doi.org/10.1016/0198-0149(82)90088-7

Menary, M. B., Jackson, L. C., & Lozier, M. S. (2020). Reconciling the relationship between the AMOC and Labrador Sea in OSNAP observations and climate models. *Geophysical Research Letters*, *47*(18), e2020GL089793. https://doi.org/10.1029/2020gl089793

Montgomery, R. B. (1937). A suggested method for representing gradient flow in isentropic surfaces. *Bulletin of the American Meteorological Society*, *18*(6/7), 210–212. https://doi.org/10.1175/1520-0477-18.6-7.210

Ortega, P., Robson, J., Sutton, R. T., & Andrews, M. B. (2017). Mechanisms of decadal variability in the Labrador Sea and the wider North Atlantic in a high-resolution climate model. *Climate Dynamics*, *49*(7), 2625–2647. https://doi.org/10.1007/s00382-016-3467-y

Robson, J., Hodson, D., Hawkins, E. D., & Sutton, R. (2014). Atlantic overturning in decline? *Nature Geoscience*, *7*(1), 2–3. https://doi.org/10.1038/ngeo2050

Robson, J., Ortega, P., & Sutton, R. (2016). A reversal of climatic trends in the North Atlantic since 2005. *Nature Geoscience*, *9*(7), 513–517. https://doi.org/10.1038/ngeo2727

Robson, J., Sutton, R., Lohmann, K., Smith, D., & Palmer, M. D. (2012). Causes of the rapid warming of the North Atlantic Ocean in the mid-1990s. *Journal of Climate*, *25*(12), 4116–4134. https://doi.org/10.1175/jcli-d-11-00443.1

Robson, J., Sutton, R., & Smith, D. (2014). Decadal predictions of the cooling and freshening of the North Atlantic in the 1960s and the role of ocean circulation. *Climate Dynamics*, *42*(9), 2353–2365. https://doi.org/10.1007/s00382-014-2115-7

Smith, D. M., Allan, R. P., Coward, A. C., Eade, R., Hyder, P., Liu, C., et al. (2015). Earth's energy imbalance since 1960 in observations and CMIP5 models. *Geophysical Research Letters*, *42*(4), 1205–1213. https://doi.org/10.1002/2014gl062669

Visbeck, M., Cullen, H., Krahmann, G., & Naik, N. (1998). An ocean model's response to North Atlantic Oscillation-like wind forcing. *Geophysical Research Letters*, *25*(24), 4521–4524. https://doi.org/10.1029/1998gl900162

Williams, R. G., Roussenov, V., Lozier, M. S., & Smith, D. (2015). Mechanisms of heat content and thermocline change in the subtropical and subpolar North Atlantic. *Journal of Climate*, *28*(24), 9803–9815. https://doi.org/10.1175/jcli-d-15-0097.1

Williams, R. G., Roussenov, V., Smith, D., & Lozier, M. S. (2014). Decadal evolution of ocean thermal anomalies in the North Atlantic: The effects of Ekman, overturning, and horizontal transport. *Journal of Climate*, *27*(2), 698–719. https://doi.org/10.1175/JCLI-D-12-00234.1

Yeager, S., & Danabasoglu, G. (2014). The origins of late-twentieth-century variations in the large-scale North Atlantic circulation. *Journal of Climate*, *27*(9), 3222–3247. https://doi.org/10.1175/jcli-d-13-00125.1

Zou, S., Lozier, M. S., & Xu, X. (2020). Latitudinal structure of the meridional Overturning circulation variability on interannual to decadal time scales in the North Atlantic Ocean. *Journal of Climate*, *33*(9), 3845–3862. https://doi.org/10.1175/JCLI-D-19_0215.1